



TITLE:

EFSO at different geographical locations verified with observing-system experiments

AUTHOR(S):

Yamazaki, Akira; Miyoshi, Takemasa; Inoue, Jun; Enomoto, Takeshi; Komori, Nobumasa

CITATION:

Yamazaki, Akira ...[et al]. EFSO at different geographical locations verified with observing-system experiments. *Weather and Forecasting* 2021, 36(4): 1219-1236

ISSUE DATE:

2021-08

URL:

<http://hdl.handle.net/2433/263913>

RIGHT:

© 2021 American Meteorological Society; 発行元の許可を得て登録しています。; The full-text file will be made open to the public on 25 December 2021 in accordance with publisher's 'Terms and Conditions for Self-Archiving'.

EFSO at Different Geographical Locations Verified with Observing System Experiments

AKIRA YAMAZAKI,^a TAKEMASA MIYOSHI,^{b,a} JUN INOUE,^{c,a} TAKESHI ENOMOTO,^{d,a} AND NOBUMASA KOMORI^a

^a Application Laboratory, JAMSTEC, Yokohama, Japan

^b RIKEN Center for Computational Science, Kobe, Japan

^c National Institute of Polar Research, Tachikawa, Japan

^d Disaster Prevention Research Institute, Kyoto University, Uji, Japan

(Manuscript received 27 August 2020, in final form 26 March 2021)

ABSTRACT: An ensemble-based forecast sensitivity to observations (EFSO) diagnosis has been implemented in an atmospheric general circulation model–ensemble Kalman filter data assimilation system to estimate the impacts of specific observations from the quasi-operational global observing system on weekly short-range forecasts. It was examined whether EFSO reasonably approximates the impacts of a subset of observations from specific geographical locations for 6-h forecasts, and how long the 6-h observation impacts can be retained during the 7-day forecast period. The reference for these forecasts was obtained from 12 data-denial experiments in each of which a subset of three radiosonde observations launched from a geographical location was excluded. The 12 locations were selected from three latitudinal bands comprising (i) four Arctic regions, (ii) four midlatitude regions in the Northern Hemisphere, and (iii) four tropical regions during the Northern Hemisphere winter of 2015/16. The estimated winter-averaged EFSO-derived observation impacts well corresponded to the 6-h observation impacts obtained by the data denials and EFSO could reasonably estimate the observation impacts by the data denials on short-range (from 6 h to 2 day) forecasts. Furthermore, during the medium-range (4–7 day) forecasts, it was found that the Arctic observations tend to seed the broadest impacts and their short-range observation impacts could be projected to beneficial impacts in Arctic and midlatitude North American areas. The midlatitude area was located just downstream of dynamical propagation from the Arctic toward the midlatitudes. Results obtained by repeated Arctic data-denial experiments were found to be generally common to those from the non-repeated experiments.


KEYWORDS: Arctic; Atmospheric circulation; Ensembles; Forecast verification/skill; Numerical weather prediction/forecasting; Short-range prediction

1. Introduction

Observing system experiments (OSEs) are commonly used for evaluating the impact of observations on data assimilation systems. OSEs enable us to quantify the impact of observations in specific regions or of type, by excluding them from or adding them to the total observations assimilated into a data assimilation system. OSEs are usually used to evaluate the direct influence of observations on weather phenomena occurring over regions at all distances, from the local to the global domains (e.g., Weissmann et al. 2011; Ito et al. 2018; Sato et al. 2017; Schäfer et al. 2018); they are also used to estimate the total impact of some observation types or observations in specific latitudinal bands on the global observing system (e.g., Bormann et al. 2019; Day et al. 2019; Lawrence et al. 2019). In previous work, we have conducted many OSEs using in-house developed data assimilation system known as the Atmospheric General Circulation Model for the Earth Simulator—a local ensemble transform Kalman filter (AFES-LETKF) ensemble data assimilation system (ALEDAS; see appendix A). This system has been used to generate an experimental atmospheric global ensemble reanalysis (ALERA2). So far, these studies

have focused on the *remote* influences of small subsets of observations obtained during field campaigns (e.g., Inoue et al. 2013; Yamazaki et al. 2015). To clarify how observation impacts propagate and where their impacts accumulate in quasi-operational data assimilation and forecast systems can provide useful information for the design of observational campaigns. However, conducting OSEs during a campaign is not very practical because they are too expensive in computational resources and time, as additional data assimilation and forecast cycles must be performed to evaluate specific observations.

Alternatively, the forecast sensitivity to observation (FSO) technique pioneered by Langland and Baker (2004) allows us to diagnose the impacts of all observations by quantifying the extent to which each observation improves or degrades subsequent forecasts. FSO estimates (diagnoses) individual observation impacts at early short-range forecast times, which are typically 6–24 h. In this study we adopt the acronym FSO instead of FSOI (forecast sensitivity observation impact) also used in many previous studies (e.g., Sommer and Weissmann 2016). The FSO formulation has been originally developed for variational data assimilation systems as the adjoint-based FSO. Recent studies by Liu and Kalnay (2008) and Kalnay et al. (2012) have applied the formulation to the ensemble Kalman filter (EnKF) system, known as the ensemble-based FSO (called EFSO). The EFSO diagnosis can be used in current data assimilation schemes. Recently, Kotsuki et al. (2019) showed the usefulness of EFSO in a nonhydrostatic model. Alongside the global NWP model, Sommer and Weissmann (2016)

 Denotes content that is immediately available upon publication as open access.

Corresponding author: Akira Yamazaki, yzaki@jamstec.go.jp

DOI: 10.1175/WAF-D-20-0152.1

© 2021 American Meteorological Society. For information regarding reuse of this content and general copyright information, consult the AMS Copyright Policy (www.ametsoc.org/PUBSReuseLicenses).

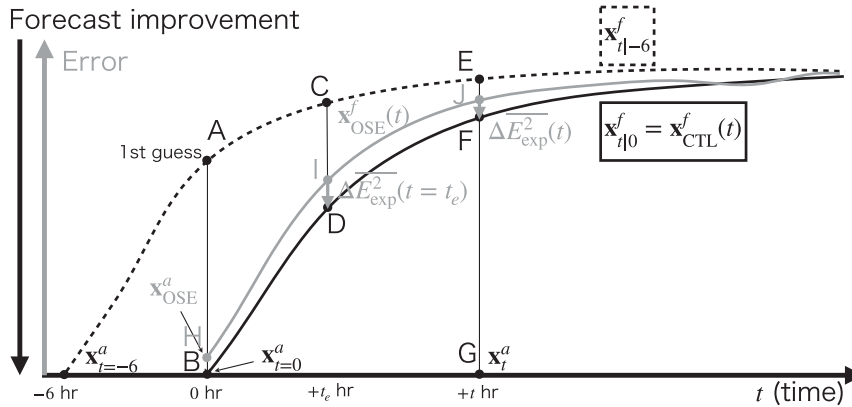


FIG. 1. Schematic of the relationship between the total OI_{OSE} (line EF) and forecast errors (or improvements, dashed and solid lines) verified against the referenced analysis at time $t \mathbf{x}_t^a$ (point G). The forecast errors $\mathbf{e}_{t|0}^T \mathbf{C} \mathbf{e}_{t|0}$ (dashed line) and $\mathbf{e}_{t|0}^T \mathbf{C} \mathbf{e}_{t|0}$ (solid line) are obtained from two forecasts $\mathbf{x}_{t|0}^f$ and $\mathbf{x}_{t|0}^f$ started from the analysis at $t = -6$ h, $\mathbf{x}_{t=-6}^a$, and from the analysis at $t = 0$ h, $\mathbf{x}_{t=0}^a$ (point B), respectively. The total OI_{OSE} at $t = t_e$ hour (evaluation lead time), $\Delta E^2(t = t_e)$ (line CD), is quantified as the difference between the forecast errors and is approximated by the sum of the OI_{EFSO} values $\sum \Delta \varepsilon^2$. Here line AB corresponds to the analysis increment. The gray colors indicate when an OSE forecast is additionally performed. The OSE forecast $\mathbf{x}_{OSE}^f(t)$ started from the OSE analysis at $t = 0$, $\mathbf{x}_{t=0}^a$ (point H), leads to the forecast error of the OSE $\mathbf{e}_{t|0}^T \mathbf{C} \mathbf{e}_{t|0}$ (gray line). In the OSE a small subset of observations is excluded. Here, $\mathbf{x}_{t|0}^f$ are equivalent to the control forecast $\mathbf{x}_{CTL}^f(t)$, which is compared with $\mathbf{x}_{t|0}^f$. Both $\mathbf{x}_{CTL}^f(t)$ and $\mathbf{x}_{t|0}^f$ are verified against \mathbf{x}_t^a . The OI_{OSE} of the subset at time t , $\Delta E_{exp}^2(t)$, is quantified by the difference between the forecast errors $\mathbf{e}_{t|0}^T \mathbf{C} \mathbf{e}_{t|0}$ and $\mathbf{e}_{t|0}^T \mathbf{C} \mathbf{e}_{t|0}$ (line JF). The OI_{OSE} at $t = t_e$ hour, $\Delta E_{exp}^2(t = t_e)$ (line ID), is approximated by the OI_{EFSO} value of the subset of the observations $\Delta \varepsilon_{exp}^2(t = t_e)$.

and Necker et al. (2018) successfully adopted the EFSO diagnosis for a convection-permitting regional model. The adjoint-based FSO and EFSO diagnoses can be used to quantify the impact of each observation individually, without the need to conduct OSEs. The adjoint-based FSO and EFSO techniques have been successfully used to estimate the impacts of specific observation types (e.g., satellite observations) against conventional ones (e.g., Gelaro and Zhu 2009). Recently, Lien et al. (2018) proposed the use of the EFSO diagnosis in an offline approach to develop new data selection strategies. Elsewhere, Ota et al. (2013) and Hotta et al. (2017) proved that the EFSO technique can be used for the proactive quality control of observations.

Previous studies used the adjoint-based FSO and EFSO techniques for targeted observations. In targeted observations (Majumdar 2016), one deploys and assimilates additional observations through an observational campaign to improve the numerical forecast of a weather event. Since targeted observations are conducted to better forecast weather events that occur near campaign sites, an FSO diagnosis that estimates a forecast impact in less than a day would be most useful. However, it is not known yet whether the adjoint-based FSO or EFSO is useful for estimating the remote impacts of observations or impacts on time scales longer than a day. This may be desirable for field campaigns conducted from ships or near-stationary mobile platforms.

In the adjoint-based FSO and EFSO context the observation impact represents the difference between a selected measure

of error on the analysis and background model state trajectories (see section 2a and Fig. 1). In this study, we define observation impacts obtained by actual data assimilation cycles (OSEs) as OI_{OSE} and those estimated by the EFSO technique which has been implemented as OI_{EFSO} .

Our purpose is to understand how well EFSO can estimate OI_{OSE} of individual observations and their downstream influence. We also aim to understand which points are most influential on short- and/or medium-range weekly forecasts; in other words, we seek to discover the “optimal spot” of observational locations to enhance global NWP forecasts. To the best of our knowledge, only a few recent studies directly compared the adjoint-based FSO and EFSO diagnoses and OI_{OSE} obtained by data-denial experiments in the global observing framework. Gelaro and Zhu (2009) compared the values obtained from the adjoint-based FSO with those obtained from data-denial experiments. For satellite observations they used the adjoint-based FSO technique to estimate the relative contributions by observation type, with a focus on conventional and satellite observations. Ota et al. (2013) conducted a data-denial experiment for a case where several satellite-wind observations that were estimated as candidates to degrade a forecast by EFSO. They showed that the estimation could capture the actual 24-h forecast change. Hotta et al. (2017) further developed the study of Ota et al. (2013) and proposed the concept of “proactive QC (quality control)” in which observations with the potential to degrade a forecast could be detected by EFSO and rejected during the data

assimilation process. Very recently, Lawrence et al. (2019) compared observation impacts estimated by the adjoint-based FSO with OI_{OSE} from data-denial experiments to study how Arctic observations influence global weather forecasts. They found that the relative contributions of observation types obtained by the adjoint-based FSO technique were consistent with the results of the data-denial experiments for short and even medium forecast ranges. The aforementioned studies illustrated that adjoint-based FSO and EFSO techniques are useful for estimating OI_{OSE} on short- and medium-range forecasts. Their focus, however, was on large numbers of globally distributed observations rather than on small subsets obtained through observational campaigns.

To demonstrate the usefulness of EFSO for evaluating OI_{OSE} on short- and medium-range forecasts and for estimating the remote impacts of localized observations obtained in field campaigns, we need to address the following question:

- Can the EFSO technique reasonably approximate the short-range OI_{OSE} obtained by data-denial experiments?

Since the adjoint-based FSO and EFSO are formulated to estimate OI_{OSE} at an early short-range forecast, it is not obvious whether the early short-range (initial) OI_{OSE} can be retained in longer forecast ranges. Privé et al. (2021) discussed time evolution of observation impacts estimated by the adjoint-based FSO, and showed that their behaviors are different between extratropical and tropical observations. Thus, discussion on mechanisms of how the initial OI_{OSE} amplify and propagate starting from observed locations at different latitudinal bands is helpful to suggest whether EFSO can be useful to short- to medium-range forecasts. The following questions are also need to be addressed:

- Are initial (at an early short-range forecast) OI_{OSE} estimated by the EFSO diagnosis are dynamically propagated in the forecast to retain their impacts on longer forecasts?
- Which is the most important for improving medium-range weather forecasts the Arctic, the midlatitudes, or the tropics?

To clarify those points, we conduct multiple data-denial experiments in which several radiosonde observations launched from various geographical locations are removed from the real global observing network. Medium-range forecast experiments (up to 7 days) are then initialized by the data-denied analysis fields to measure OI_{OSE} and subsequently compared with OI_{EFSO} . We focus on the impacts of radiosonde observations because they are the most reliable observation type and include both the lower and upper atmospheric state; they are also more robust than satellite observations, in the sense that they do not strongly depend on seasons and weather conditions. Nonetheless, the knowledge and methods obtained in this study should be applicable to other observation types. Our results suggest that the planning of observational campaigns could benefit from the use of the EFSO technique. To the best of our knowledge, this is the first study to investigate how well EFSO can estimate OI_{OSE} derived from multiple data-denial experiments for various locations selected wholly from a global domain. The paper is organized as follows. Section 2 introduces the formulation of the ensemble-based FSO (EFSO), and the

implementation of this technique in ALEDAS. Section 3 introduces experimental designs of data-denial experiments (OSEs). In section 4, first, OI_{EFSO} are compared with OI_{OSE} in the short-range forecast. Second, we investigate how to propagate OI_{OSE} in each OSE during the medium-range forecast. Last, it is discussed whether EFSO can be useful to estimate OI_{OSE} by repeated OSEs that mimics long-lasting near-stationary observational campaigns. Section 5 discusses the summary and our speculations.

2. Implementation of EFSO in ALEDAS

ALEDAS is a global atmospheric data assimilation system that combines AFES (an AGCM) with the LETKF (an EnKF). See appendix A for detailed configurations.

a. Physical interpretation of the observation impact and its approximation by EFSO

In this subsection, we define the observation impact, give a physical interpretation, and discuss how it can be approximated by the EFSO technique. The details of the EFSO formulation are available in Kalnay et al. (2012), Ota et al. (2013), and Hotta et al. (2017).

1) THE TOTAL OBSERVATION IMPACT (TOTAL OI_{OSE})

First, we define the total OI_{OSE} at time t , which is the area average of OI_{OSE} for a target domain, $\Delta\bar{E}^2(t)$, quantified by the difference between the forecast errors initialized 6 h before the analysis time $t = 0$, \mathbf{e}_{t-6} , and initialized at $t = 0$, \mathbf{e}_{t0} :

$$\Delta\bar{E}^2(t) \equiv \mathbf{e}_{t-6}^T \mathbf{C} \mathbf{e}_{t-6} - \mathbf{e}_{t0}^T \mathbf{C} \mathbf{e}_{t0} = -(\mathbf{x}_{t0}^f - \mathbf{x}_{t-6}^f)^T \mathbf{C} (\mathbf{e}_{t0} + \mathbf{e}_{t-6}), \quad (1)$$

where $\mathbf{e}_{t0} \equiv \mathbf{x}_{t0}^f - \mathbf{x}_t^v$, $\mathbf{e}_{t-6} \equiv \mathbf{x}_{t-6}^f - \mathbf{x}_t^v$, and \mathbf{C} is a matrix that defines an energy norm and an area-averaged operation. The terms \mathbf{x}_{t0}^f and \mathbf{x}_{t-6}^f represent the ensemble-mean forecast from the analyzed time ($t = 0$) and 6 h before ($t = -6$) to the verifying time t ; \mathbf{x}_t^v is the reference (truth) verifying forecast errors. The terms \mathbf{x} and \mathbf{e} are the state vectors for the target domain. In this study, our reference is the ensemble mean of the analysis $\mathbf{x}_t^v \equiv \mathbf{x}_t^a$. The meaning of $\Delta\bar{E}^2(t)$ (total OI_{OSE}) is conceptualized in Fig. 1. Total OI_{OSE} quantifies how close (similar) \mathbf{x}_{t0}^f and \mathbf{x}_{t-6}^f are to \mathbf{x}_t^a and how large the difference between \mathbf{x}_{t0}^f and \mathbf{x}_{t-6}^f is. If \mathbf{x}_{t-6}^f is closer to \mathbf{x}_t^a than \mathbf{x}_{t0}^f over the target domain, $\Delta\bar{E}^2(t)$ becomes negative. At $t = 0$, the total OI_{OSE} $\Delta\bar{E}^2(t = 0)$ is equivalent to the analysis increment (line AB in Fig. 1). Whereas at $t \rightarrow \infty$, the total OI_{OSE} approaches to zero (Privé et al. 2021, their Fig. 5).

The total OI_{OSE} at the evaluation lead time t_e obtained by the difference between \mathbf{x}_{t0}^f and \mathbf{x}_{t-6}^f , $\Delta\bar{E}^2(t = t_e)$, is expressed as the “ t_e -hour” total OI_{OSE} .

2) THE EFSO APPROXIMATION

Second, we explain how OI_{EFSO} can be estimated through the use of the EFSO technique. $\Delta\bar{E}^2(t = t_e)$ is diagnosed through the sum of the OI_{EFSO} values $\sum \Delta\bar{e}^2(t = t_e)$ in the following way. In Eq. (1), by assuming $\mathbf{x}_t^v = \mathbf{x}_t^a$, we can obtain $(\mathbf{e}_{t0} + \mathbf{e}_{t-6})$. Normally, one would now use the adjoint model to solve

$(\mathbf{x}_{i0}^f - \mathbf{x}_{i-6}^f)^T$. The EFSO formulation, however, enables the calculation of this term without the expensive calculation of the adjoint model. This is done by alternatively using the ensemble forecast at t , \mathbf{X}_{i0}^f , and the ensemble perturbation at $t = 0$ in observation space \mathbf{Y}_0^a , which approximates the Kalman gain (Kalnay et al. 2012):

$$\sum \Delta \bar{\varepsilon}^2(t) = -(\delta \mathbf{y}_0^{\text{ob}})^T \frac{1}{K-1} \rho^\circ \left[\mathbf{R}^{-1} \mathbf{Y}_0^a (\mathbf{X}_{i0}^f)^T \right] \mathbf{C} (\mathbf{e}_{i0} + \mathbf{e}_{i-6}), \quad (2)$$

where $\delta \mathbf{y}_0^{\text{ob}}$ is the observation-minus-background (O-B) innovation of the ensemble mean ($\delta \mathbf{y}_0^{\text{ob}} = \mathbf{y} - H \mathbf{x}_{0-6}^f$, where \mathbf{y} and $H \mathbf{x}_{0-6}^f$ are observation and the ensemble-mean forecast from $t = -6$ to $t = 0$ in observation space, respectively), K is the ensemble size, \mathbf{R} is the observation error matrix, \mathbf{X}_{i0}^f is the ensemble perturbation matrix of \mathbf{x}_{i0}^f ; here, \circ and ρ are the Schur product and localization matrix, which define the localization function same as that used in the LETKF of ALEDAS. Note that observations with positive or beneficial (negative or nonbeneficial) $\Delta \bar{\varepsilon}^2(t = t_e)$ or $\sum \Delta \bar{\varepsilon}^2(t = t_e)$ in Eqs. (1) and (2) are expected to improve (degrade) a subsequent forecast.¹

Because $\delta \mathbf{y}_0^{\text{ob}}$ is a vector composed of individual observations, we can decompose $\sum \Delta \bar{\varepsilon}^2(t)$ into each observation's OI_{EFSO} value. Here, $\sum \Delta \bar{\varepsilon}^2(t = t_e)$ is sum of $\Delta \bar{\varepsilon}^2(t = t_e)$ and approximates $\Delta \bar{\varepsilon}^2(t = t_e)$. A decomposed t_e -hour OI_{EFSO} value for an observation estimates a t_e -hour OI_{OSE} , which is obtained by conducting a data-denial (or an OSE) experiment of the observation (Fig. 1).

3) THE MATRIX \mathbf{C} AND THE DIFFERENCE BETWEEN THE FORECAST ERRORS

Last, we define OI_{OSE} at a grid point, $\Delta E^2(t)$. As the matrix \mathbf{C} , we adopt the vertically summed moist total energy error norm (Ota et al. 2013; Hotta et al. 2017; Kotsuki et al. 2019), which includes an area weighting function of latitude. The area average of $\Delta E^2(t)$ over the target domain is equivalent to $\Delta \bar{\varepsilon}^2(t)$ because of the weighting function. From the definition of Eq. (1):

$$\Delta E^2(t) \equiv -\frac{1}{2} \frac{1}{p_s} \int_{p_s}^0 (u^2 + v^2) + \frac{c_p}{T_r} T^2 + \frac{L^2}{c_p T_r} q^2 dp + \frac{R_d T_r}{p_r} p_s^2, \quad (3)$$

where p is the vertical pressure coordinate; p_s is the surface pressure; u, v, T, q , and p_s are the zonal wind, meridional wind, temperature, specific humidity, and surface pressure, respectively; c_p is the specific heat capacity of the air; R_d is the gas constant of dry air; L is the latent heat of condensation per unit mass; and T_r and p_r are the reference temperature and surface pressure, respectively. Here, the ‘‘difference’’ (or sensitivity) is defined as

$$x^2 = -(\mathbf{x}_{i0}^f - \mathbf{x}_{i-6}^f)(\mathbf{e}_{i0} + \mathbf{e}_{i-6}), \quad (4)$$

¹ Note that the sign of our definition of $\Delta \bar{\varepsilon}^2(t)$ is opposite to that in some previous studies.

where $x(e)$ is an element of $\mathbf{x}(e)$ and is identical to u, v, T, q , or p_s . If x_{i-6}^f is closer to x_i^a than x_{i0}^f at the grid point, $\Delta E^2(t)$ becomes negative.

b. Implementation

To calculate OI_{EFSO} , we need to select several parameters. The target domain of EFSO is set to the global domain. The evaluation lead time t_e is mainly set to 6 h. The moving localization scheme (Ota et al. 2013; Hotta et al. 2017) with coefficient 1.0 is adopted, in which the localization function is advected by the wind fields of \mathbf{x}_0^a and \mathbf{x}_e^a (i.e., \mathbf{x}_e^a) multiplied by a weighting coefficient between 0 and 1. Those EFSO parameters are selected based on practical considerations that we explain below.

In this paper, we use as our reference \mathbf{x}^a the ensemble mean of the analysis, although some recent studies suggested that the observation should be used (Cardinali 2018; Necker et al. 2018; Kotsuki et al. 2019; Privé et al. 2021). The rationale is that we would like to use the EFSO diagnosis as an alternative to OSE, mainly because OSEs are normally compared against their own analysis. In addition, as shown in Fig. A1, ALERA2 (analysis) reproduces reasonably well the synoptic and general circulations that we are interested in. EFSO is also sensitive to the error metric (Necker et al. 2018; Kotsuki et al. 2019) and the target domain used. Our choice of using the error metric [Eq. (3)] and the target area (global domain) is typical for EFSO and the adjoint-based FSO studies and serves to emphasize the forecast errors in the densely populated midlatitudes.

The reasons for evaluating at lead time 6 h rather than at longer ones are as follows.

- The 6-h EFSO has a much lower computational cost. An additional process that one substantially uses to calculate is extended forecasts for 3 h (See appendix A).
- The 6-h EFSO suffers less from the impact of the moving localization scheme than EFSO with longer evaluation (lead) times (Hotta et al. 2017; Kotsuki et al. 2019). It would be difficult to determine the optimal weighting coefficient of the moving localization, since OI_{EFSO} can be propagated in the Lagrangian way and by the Rossby wave transport owing to phase and group velocity (Kalnay et al. 2012). For example, Ota et al. (2013) chose the coefficient 0.75 for 24-h EFSO in an operational global data-assimilation system.

c. Evaluation

We first examine whether the implemented EFSO technique works correctly in ALEDAS. ALEDAS forecast–analysis cycles with EFSO diagnoses are examined for the period of December–February 2015/16 (Fig. 2).

Total $\text{OI}_{\text{EFSO}} \sum \Delta \bar{\varepsilon}^2(t = 6)$ can estimate $\Delta \bar{\varepsilon}^2(t = 6)$ similar to the previous adjoint-based FSO and EFSO studies, as evidenced by the winter average of $\sum \Delta \bar{\varepsilon}^2(t = 6)$ (2.42 J kg^{-1}), which is mostly the same as the winter average of $\Delta \bar{\varepsilon}^2(t = 6)$ (2.82); the daily variation of $\sum \Delta \bar{\varepsilon}^2(t = 6)$ is also highly correlated with that of $\Delta \bar{\varepsilon}^2(t = 6)$ (0.95). Both the average difference and the correlation are consistent with OI_{EFSO} in Ota et al. (2013), Hotta et al. (2017), and Kotsuki et al. (2019), and the total OI_{EFSO} slightly underestimates the total OI_{OSE} in the

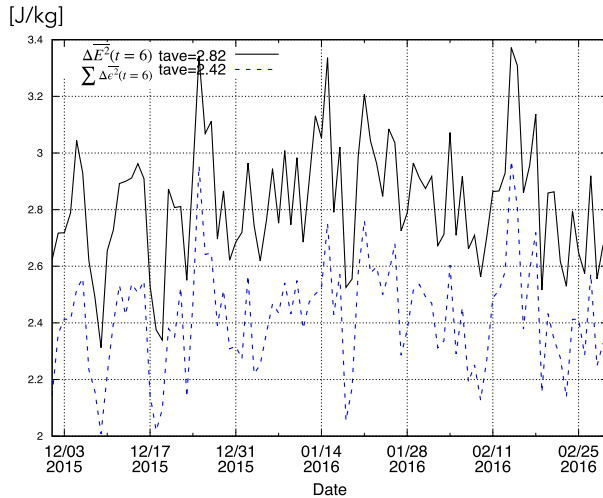


FIG. 2. Time series of the sum of the 6-h total OI_{EFSO} values $\sum \Delta \varepsilon^2$ ($J\ kg^{-1}$; blue dashed) and the 6-h total OI_{OSE} $\Delta E^2(t=6)$ (black) for every 0000 UTC during the period of December 2015–February 2016. It is important to note that the 6-h total OI_{OSE} $\Delta E^2(t=6)$ is calculated by Eq. (4) as the difference between the 12-h forecast and the first guess (6-h forecast) fields (Fig. A2).

same sense as Kotsuki et al. (2019) (EFSO) and Privé et al. (2021) (the adjoint-based FSO), implying that the EFSO diagnosis works accurately when implemented in ALEDAS.

The distribution map of the winter-averaged OI_{EFSO} values $\Delta \varepsilon^2(t=6)$ for radiosonde observations in the Northern Hemisphere and the tropics is shown in Fig. 3. OI_{EFSO} is greater where the radiosonde observation density is lower. When comparing the OI_{EFSO} values in the latitudinal direction, generally the values become larger at the higher latitudes (see Fig. 16c and appendix B). In addition, Fig. 3 shows that the time-averaged impacts are distributed smoothly (i.e., not too localized). Therefore, the global distribution of $\Delta \varepsilon^2(t=6)$ of global routine observations provides information on regions

where field campaigns might have the largest impact. We note that observational campaigns may temporally modify the global distribution. However, those OI_{EFSO} features are kept during such observational campaigns when the extra radiosonde observations in the Arctic or the Antarctic regions are performed (see appendix B).

3. Experimental designs

To use the EFSO diagnosis as an alternative to an OSE, the extent to which a 6-h EFSO can estimate the individual OI_{OSE} for short- and medium-range forecasts must be examined. In this study, we conduct multiple data-denial experiments for various regions in the Northern Hemisphere and in the tropics, where radiosondes are routinely launched.

The experiments are conducted from 1 December 2015 to 29 February 2016. During this period, 7-day ensemble forecasts are initialized every day from 0000 UTC using ALERA2 (Fig. 4); that is, 91 times of 7-day forecast experiments (Fig. 4). This is our control experiment (CTL hereafter).

We compare CTL with 12 data-denial experiments (OSEs). In each of these experiments, a subset of radiosonde observations from three adjacent sites is excluded. Four locations are in the midlatitudes (20° – $60^\circ N$), four in the Arctic (60° – $90^\circ N$), and four in the tropics ($10^\circ S$ – $10^\circ N$), as shown in Fig. 5. The midlatitude locations are hereafter denoted as the Mid, Mid2, Mid3, and Mid4 experiments (black symbols in Fig. 5); the Arctic locations as Pol, Pol2, Pol3, and Pol4 experiments (blue symbols); and the tropical locations as Tro, Tro2, Tro3, and Tro4 experiments (red symbols). After the data denial, 7-day ensemble forecasts are initialized every day from 0000 UTC using OSE analyses (Fig. 4); that is, 91 times of 7-day forecast experiments for each OSE. Note that the data denial in the data assimilation process is not repeated to avoid the temporal accumulation of OI_{OSE} ; i.e., the data denial is only performed once before each forecast. These non-repeated data-denial experiments will help us to understand how OI_{OSE} propagate dynamically. Each CTL and OSE ensemble forecast is

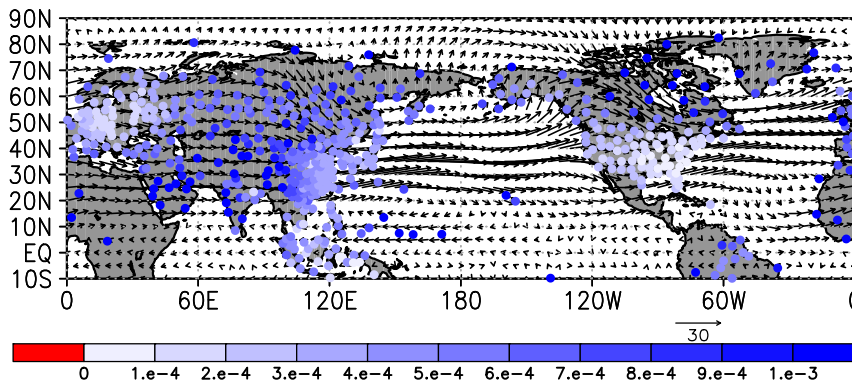


FIG. 3. The winter-averaged OI_{EFSO} values $\Delta \varepsilon^2(t=6)$ per cycle ($J\ kg^{-1}$) for global radiosonde observations and the analyzed vertically averaged wind field ($m\ s^{-1}$) in ALERA2. Note that only radiosonde observations for locations that reported more than 80 times at 0000 UTC during the cycling period (winter) are shown. (Total number of the radiosonde observations at each site is 91.)

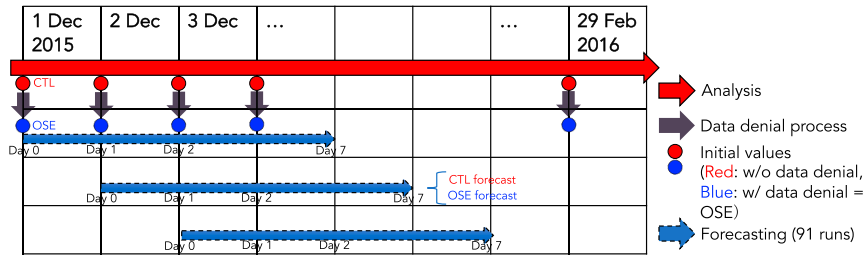


FIG. 4. Schematic of the experimental designs. The solid red arrow denotes the forecast–analysis (data assimilation) cycle of ALERA2, and the dashed blue arrows indicate the 7-day ensemble forecast experiments initialized with ALERA2 (red circles, CTL experiments) and the data-denied analyses by each OSE (blue circles). The number of OSEs is 12, that is, the Mid, Mid2, Mid3, Mid4, Pol, Pol2, Pol3, Pol4, Tro, Tro2, Tro3, and Tro4 experiments. The 7-day forecast experiments started every day at 0000 UTC during winter; and in total, the experiments were conducted 91 times. Each ensemble forecast (each dashed blue arrow) includes two ensemble forecasts, initialized from the 63-member CTL and OSE analyses.

initialized from the 63 members of the CTL (ALERA2) and OSE analyses. To evaluate the OI_{OSE} in each OSE, we compare the ensemble forecast mean of CTL $\mathbf{x}_{CTL}^f(t)$ with that of the OSE $\mathbf{x}_{OSE}^f(t)$. This is because for the definition of EFSO the ensemble mean is used (for $\mathbf{e}_{|0}$ and $\mathbf{e}_{|6}$).

We define the OI_{OSE} of the excluded (denied) radiosondes for the global domain, $\Delta E_{exp}^2(t)$, as the differences between $\mathbf{x}_{CTL}^f(t)$ and $\mathbf{x}_{OSE}^f(t)$:

$$\begin{aligned} \Delta E_{exp}^2(t) &= \mathbf{e}_{OSE}^T(t) \mathbf{C} \mathbf{e}_{OSE}(t) - \mathbf{e}_{CTL}^T(t) \mathbf{C} \mathbf{e}_{CTL}(t) \\ &= -[\mathbf{x}_{CTL}^f(t) - \mathbf{x}_{OSE}^f(t)]^T \mathbf{C} [\mathbf{e}_{CTL}(t) + \mathbf{e}_{OSE}(t)], \end{aligned} \quad (5)$$

where $\mathbf{e}_{OSE}(t) \equiv \mathbf{x}_{OSE}^f(t) - \mathbf{x}_t^a$ and $\mathbf{e}_{CTL}(t) \equiv \mathbf{x}_{CTL}^f(t) - \mathbf{x}_t^a$ (Fig. 1) are calculated for lead times from 6 h to 7 days. Also, $\Delta E_{exp}^2(t)$ at each grid point, $\Delta E_{exp}^2(t)$ is calculated in the same way as Eqs. (3) and (4). The relationship between $\Delta E_{exp}^2(t)$ and $\Delta E^2(t)$ is schematically shown in Fig. 1: $\Delta E_{exp}^2(t)$ is an component of $\Delta E^2(t)$ (i.e., point J is located on line EF). Also, point H \mathbf{x}_{OSE}^a (the initial value of the OSE) is near point B \mathbf{x}_{CTL}^a (the initial value of the CTL or \mathbf{x}_0^a) and on the line connecting points A and B.

The OI_{EFSO} of a specific OSE $\Delta \overline{\mathbf{e}_{exp}^2}(t)$ and $\Delta \mathbf{e}_{exp}^2(t)$ are derived from Eq. (2) by replacing $\delta \mathbf{y}_0^{ob}$ with $\delta \mathbf{y}_0^{ob, deny}$ whose elements are set to 0 except those of the observations denied in the OSE (Hotta 2014). Thus, $\Delta \mathbf{e}_{exp}^2(t)$ approximates $\Delta E_{exp}^2(t)$ and also composes $\sum \Delta \overline{\mathbf{e}_{exp}^2}(t)$, and the area average of $\Delta \mathbf{e}_{exp}^2(t)$ over the target domain is equivalent to $\Delta \overline{\mathbf{e}_{exp}^2}(t)$.

We first compare $\Delta \overline{\mathbf{e}_{exp}^2}(t=6)$ of the subsets of the radiosondes with $\Delta \overline{E_{exp}^2}(t=6)$. Subsequently, we show how long and to what extent the 6-h EFSO diagnosis is useful for the estimation of $\Delta \overline{E_{exp}^2}(t)$ for short- and/or medium-range forecasts.

4. Results

a. Comparison of OI_{OSE} and OI_{EFSO}

We compare the 6-h OI_{EFSO} $\Delta \overline{\mathbf{e}_{exp}^2}(t=6)$ with the 6-h OI_{OSE} $\Delta \overline{E_{exp}^2}(t=6)$ (Fig. 6). In this study, we focus on comparison of the winter-averaged observation impacts rather than their daily variations, since we are interested in observation impacts which can remain in short- to medium-range forecasts; such impacts must last long enough to be reflected in the seasonal averages. These averages can be useful for deciding the

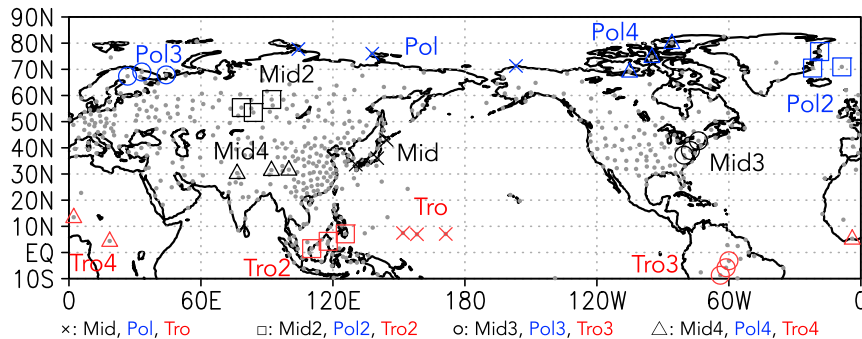


FIG. 5. Twelve observation locations (×, □, ○, and △ symbols) consisting of three routine radiosonde sites at the midlatitude (black), the Arctic (blue), and the tropical (red) bands of the OSE experiments. For each band, four locations denoted by the ×, □, ○, and △ symbols were selected. Gray dots denote all the radiosonde observation points in the Northern Hemisphere and tropics displayed in Fig. 3.

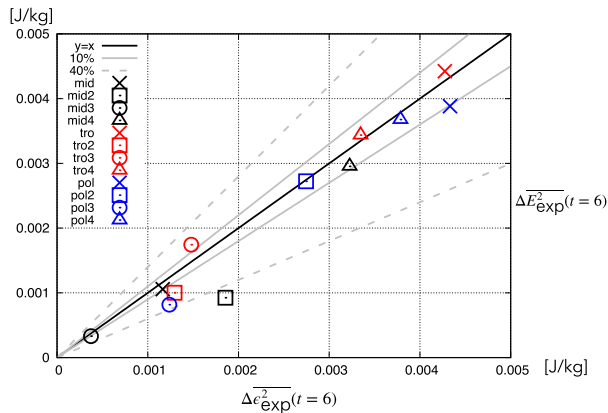


FIG. 6. Scatter diagram of $\overline{\Delta E_{\text{exp}}^2}(t=6)$ (horizontal axis) and $\overline{\Delta E_{\text{exp}}^2}(t=6)$ (vertical axis) of each experiment averaged for the 91-time forecasts (over the winter period). Colors and symbols are the same as Fig. 5 (black for the midlatitude, blue for the Arctic, and red for the tropical OSEs). The black line indicates the $y = x$ function, and the gray solid and dashed lines indicate 10% and 40% deviations from $y = x$.

location of medium-term field campaigns, such as those in the Year of Polar Prediction (YOPP, see appendix B). Hereafter we merely refer to the winter-averaged OI_{EFSO} (winter-averaged OI_{OSE}) as OI_{EFSO} (OI_{OSE}). The OI_{EFSO} values show a linear relation with $\overline{\Delta E_{\text{exp}}^2}(t=6)$ (12 plots), with the 12 points close to the $y = x$ line. All of the points are within 40% deviation from the line except Mid2 and most (8 of the 12) points are within 10%, indicating that the EFSO technique can estimate $\overline{\Delta E_{\text{exp}}^2}(t=6)$ except Mid2. We note that all OI_{OSE} are beneficial, which suggests that the radiosondes can always improve the subsequent forecasts. Moreover, the magnitudes of $\overline{\Delta E_{\text{exp}}^2}(t=6)$ are not sensitive to the latitudinal band. This is because we selected the denied observations for the OSEs with various OI_{EFSO} values at each latitudinal band (Fig. 3), though 6-h OI_{EFSO} values are in general larger in the polar latitudinal bands than those in the midlatitude and tropical bands (see Figs. 16c and B1).

To elucidate to what extent EFSO has potential to estimate OI_{OSE} within short-range forecasts, we compare $\overline{\Delta E_{\text{exp}}^2}(t)$ at the evaluation time $t = t_e$ with $\overline{\Delta E_{\text{exp}}^2}(t)$ from 6 to 48 h. Figure 7 shows the ratios of $\overline{\Delta E_{\text{exp}}^2}(t)$ to $\overline{\Delta E_{\text{exp}}^2}(t)$ at different evaluation times. As plotted point of an experiment is closer to 1 at t hours, t -hour EFSO better estimates OI_{OSE} . Among the different evaluation times, EFSO at $t = 6$ and 12 h can best estimate $\overline{\Delta E_{\text{exp}}^2}(t)$. This result suggests that 6-h EFSO can be more useful than 24 h or longer-hour EFSO and as useful as 12-h EFSO to estimate OI_{OSE} in ALEDAS. At the evaluation times increase, the ratios of all the experiments increase. After $t = 24$ h, $\overline{\Delta E_{\text{exp}}^2}(t)$ tends to underestimate $\overline{\Delta E_{\text{exp}}^2}(t)$, indicating that EFSO becomes meaningless to directly approximate OI_{OSE} .

In the next step, we examine whether the 6-h EFSO-derived $\overline{\Delta E_{\text{exp}}^2}(t=6)$ can be useful to estimate $\overline{\Delta E_{\text{exp}}^2}(t)$ at longer lead times (i.e., on the 12-h to 7-day forecasts). Since $\overline{\Delta E_{\text{exp}}^2}(t=6)$ specifically estimates $\overline{\Delta E_{\text{exp}}^2}(t=6)$, the examination is reworded as whether $\overline{\Delta E_{\text{exp}}^2}(t=6)$ can be projected to $\overline{\Delta E_{\text{exp}}^2}(t)$ at different lead times, or how long initial OI_{OSE} can remain against

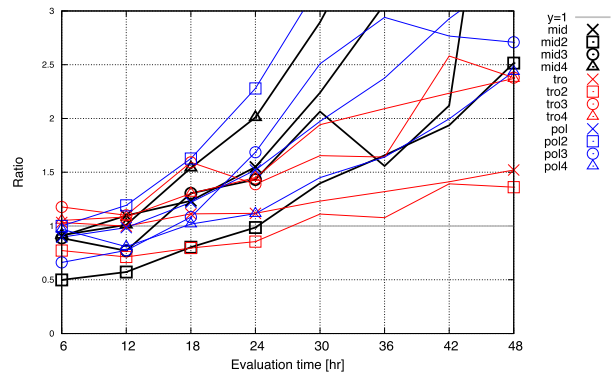


FIG. 7. Ratios of $\text{OI}_{\text{OSE}} \overline{\Delta E_{\text{exp}}^2}(t)$ to $\text{OI}_{\text{EFSO}} \overline{\Delta E_{\text{exp}}^2}(t)$ of each experiment at different evaluation times ($t = 6\text{--}48$ h). Colors and symbols are the same as Fig. 5. The gray line indicates the $y = 1$ function.

the forecast error (Privé et al. 2021). For this data analysis we extend the lead time t for $\overline{\Delta E_{\text{exp}}^2}(t)$ from 6 h to 7 days.

Figure 8 shows the time sequences of $\overline{\Delta E_{\text{exp}}^2}(t)$ (OI_{OSE}) for lead times up to 7 days at each latitudinal band (Arctic, midlatitude, or tropical). During short-range forecasts, the Arctic and midlatitude OI_{OSE} keep amplifying, while the tropical OI_{OSE} earlier amplify and keep their values after lead time of 1 day: These are consistent with different behaviors of increasing observation impacts between extratropical and tropical observations found in Privé et al. (2021). In our experiments, the Arctic OI_{OSE} more strongly amplify than the midlatitude OI_{OSE} . Note that $\overline{\Delta E_{\text{Mid2}}^2}(t)$ most strongly amplifies among the midlatitude OI_{OSE} : the observed location of Mid2 is nearest to the Arctic (Fig. 5).

The figure reveals that among each latitudinal band (each color in Fig. 8) the relative differences (rankings) of the 6-h (initial) OI_{OSE} remain unchanged up to lead times of 1 to 2 days except for Mid2. Only the relative ranking of $\overline{\Delta E_{\text{Mid2}}^2}(t)$ is not retained and cannot be estimated by 6-h EFSO. This could be because $\overline{\Delta E_{\text{Mid2}}^2}(t)$ amplifies too slowly at early short-range forecast times among the 12 OSEs (Fig. 8), and only $\overline{\Delta E_{\text{Mid2}}^2}(t=6)$ largely departs from $\overline{\Delta E_{\text{Mid2}}^2}(t=6)$, as indicated by Fig. 6. Overall, this result and Fig. 6 suggest that the 6-h EFSO can be useful for the estimation of initial OI_{OSE} and amplification of OI_{OSE} within a short-range forecast.

Starting from lead times of 3 days, however, the relative rankings do not remain intact as the time series of $\overline{\Delta E_{\text{exp}}^2}(t)$ vary drastically for almost all the experiments, with many of them dipping to negative values. Thus, EFSO cannot directly estimate $\overline{\Delta E_{\text{exp}}^2}(t)$ for medium-range forecast in the sense of the globally averaged OI_{OSE} . It should again be noted that $\overline{\Delta E_{\text{exp}}^2}(t)$ denotes the global average of $\overline{\Delta E_{\text{exp}}^2}(t)$.

It is worth mentioning that $\overline{\Delta E_{\text{exp}}^2}(t)$ is gradually increasing in whole until 7 days for almost all OSEs (see Fig. 1). It may reflect that OI_{OSE} in some areas of the global domain amplify and survive against the forecast error growth until the 7-day forecast period (Privé et al. 2021, their Fig. 5). Therefore, OI_{OSE} without the global averaging can be useful for short- to medium-range forecasts. We note that the ensemble spread of the CTL forecast also does not reach saturation over the 7-day forecast period (not shown). For operational forecasts, Zhang et al. (2019) have

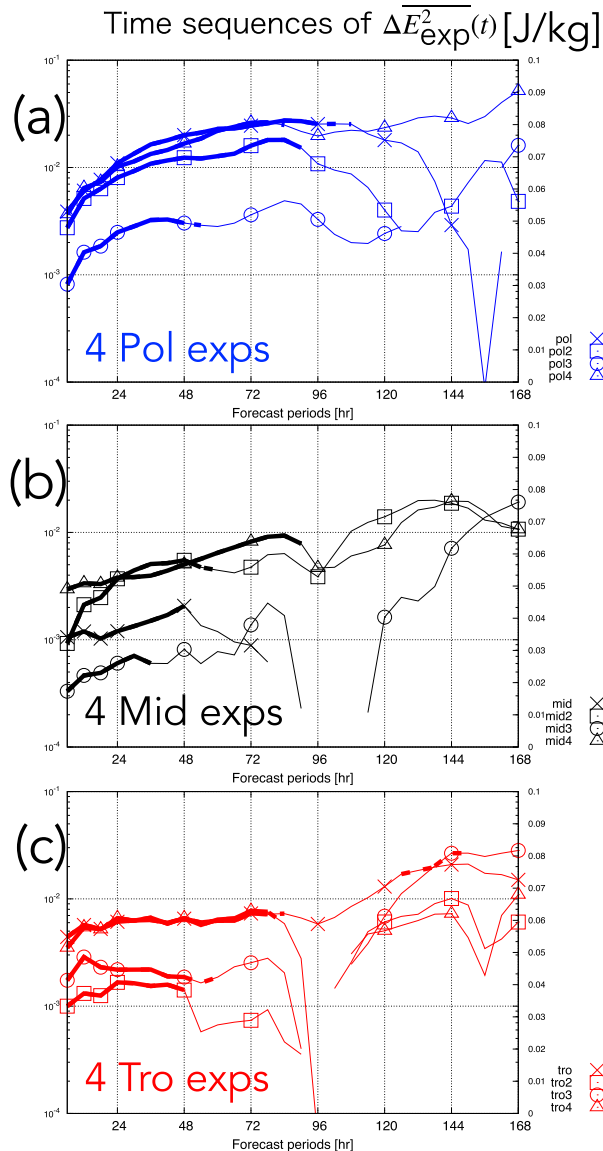


FIG. 8. Time sequences of $\text{OI}_{\text{OSE}} \Delta E_{\text{exp}}^2(t)$ (J kg^{-1}) from 6-h to 7-day forecast periods (h) for the (a) Arctic, (b) midlatitude, and (c) tropical OSEs. Colors and symbols are the same as in Fig. 5. The OI_{OSE} at the 6-h forecasts (symbols at the leftmost fringe) correspond to $\Delta E_{\text{exp}}^2(t=6)$ in Fig. 6. Deficits indicate negative values. Thick solid and dashed lines indicate statistical confidence exceeding 99% and 95% significant levels against the 91-time forecasts, respectively.

reported error saturation at around 10 days. For longer lead times, however, it should approach zero as the forecast error saturates and OI_{OSE} become meaningless.

b. Propagation of OI_{OSE}

The results so far indicate that, for short-range forecasts, EFSO is useful to estimate the globally averaged OI_{OSE} , but not for medium-range forecasts. However, when we focus on the distributions of OI_{OSE} in medium ranges, that is, $\Delta E_{\text{exp}}^2(t)$ before spatial averaging to obtain $\Delta \overline{E_{\text{exp}}^2}(t)$, the OI_{OSE} in some areas can

be projected from the magnitudes of the initial (6-h) OI_{OSE} . In this subsection, we examine horizontal maps to investigate how the observation impact of each experiment spreads out in the Northern Hemisphere. Our aim is to find out why OI_{EFSO} or the initial OI_{OSE} cannot predict $\Delta \overline{E_{\text{exp}}^2}(t)$ for medium-range forecasts (Fig. 8), and whether they can predict $\Delta E_{\text{exp}}^2(t)$ in this range.

First, we examine the temporal evolution of $\text{OI}_{\text{OSE}} [\Delta E_{\text{exp}}^2(t)]$. Initially, we focus on the three experiments Pol, Mid4, and Tro, because they show the largest 6-h OI_{EFSO} values or 6-h OI_{OSE} within their latitudinal band (symbols closest to the upper rightmost fringes in Fig. 6). Figures 9 and 11 show the evolution for 1-day (Day 1) to 7-day (Day 7) forecasts. We discover that on Day 1, OI_{EFSO} extends near the observed location in each OSE.

During the short-range and the early medium-range forecasts (Days 1–3), beneficial OI_{OSE} mainly propagates dynamically; in other words, they are propagated in the Lagrangian way (by wind advection) and by the Rossby wave transport owing to phase and group velocity (Moteki et al. 2011; Inoue et al. 2013; Yamazaki et al. 2015; Hattori et al. 2017; Sato et al. 2020b). We, hereafter, refer to this mechanism as dynamical propagation. In the Pol experiment, initial OI_{OSE} in northern East Siberia propagates southward and eastward and extends over the Arctic Ocean. In the Mid4 experiment, initial OI_{OSE} propagates eastward (downstream) with the westerly jet. In the Tro experiment, initial OI_{OSE} over the western central Pacific shifts westward with the prevailing trade winds. All these patterns are consistent with dynamical propagation.

Again to justify OI_{EFSO} , we compare the distributions of $\Delta e_{\text{exp}}^2(t)$ and $\Delta E_{\text{exp}}^2(t)$ for Day 1 to Day 3 (Fig. 10). In the three experiments, EFSO can approximate the distributions at Day 1 and to some extent at Day 2, though $\Delta e_{\text{exp}}^2(t)$ underestimate the amplitudes of OI_{OSE} as implied by Fig. 7. Thus, EFSO can estimate the dynamical propagation of OI_{OSE} within 24 forecast hours. This supports that EFSO is useful to estimate the initial amplitudes and subsequent dynamical propagation of OI_{OSE} during the short-range forecast.

In the medium range (Figs. 11a–c), however, many spots of nonbeneficial OI_{OSE} appear and both beneficial and nonbeneficial OI_{OSE} grow in the midlatitudes after Day 4, regardless of the latitudinal band of the data denial. This explains the sign changes of the globally averaged $\Delta E_{\text{exp}}^2(t)$, i.e., $\Delta \overline{E_{\text{exp}}^2}(t)$ during the medium-range forecast (Fig. 8).

During the medium range, the regions of amplified OI_{OSE} irrespective of beneficial or nonbeneficial ones seem to be concentrated in the midlatitudes, because standard deviations of $\Delta E_{\text{exp}}^2(t)$ against the 91-time forecasts have peaks around the midlatitudes, regardless of the latitudinal bands of data denial (Figs. 11d–f). When comparing the standard-deviation maps of the Mid4 and Tro experiments, the amplified regions seem to concentrate over the westerlies, including the Pacific, North America, and the Atlantic, where the Northern Hemisphere storm tracks are active (e.g., Hoskins and Hodges 2002). The storm-track activity can enhance a chaotic nature of the general atmospheric circulation, which causes the rapid growth of errors and the contamination of OI_{OSE} (Hodyss and Majumdar 2007; Sellwood et al. 2008; Ansell et al. 2018).

The beneficial and nonbeneficial OI_{OSE} in the Pol experiment in medium range broadly extend throughout the Arctic

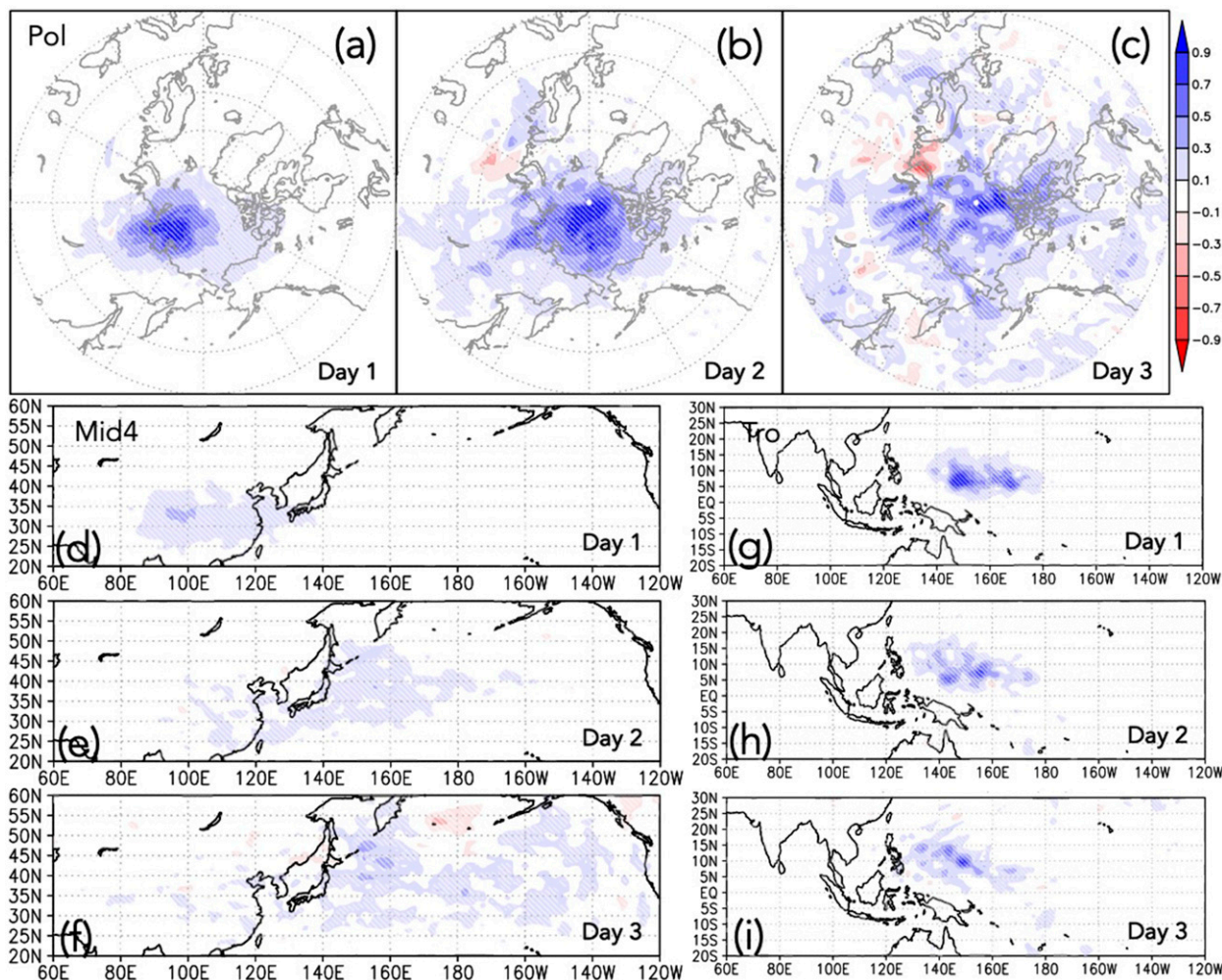


FIG. 9. Horizontal maps of $OI_{OSE} \Delta E_{exp}^2(t)$ ($J kg^{-1}$) at 1–3-day forecast times. The observation impacts of the three OSEs—(a)–(c) the Pol (blue \times in Fig. 6), (d)–(f) the Mid4 (black Δ), and (g)–(i) the Tro (red \times) experiments—are displayed. The hatching indicates statistical confidence exceeding 95%.

and toward the midlatitudes (Figs. 11a,d), and beneficial OI_{OSE} are distributed in the midlatitudes more broadly than those in the Mid4 and Tro experiments (Figs. 11a–c). Therefore, Arctic observations can be the most influential and can have broadest beneficial OI_{OSE} regions even for medium-range forecasts. If the amplified initial OI_{OSE} by the Arctic observations systematically propagates via dynamical propagation toward the midlatitudes, beneficial OI_{OSE} areas can appear downstream of the propagation in the midlatitudes.

Dynamical propagation of the OI_{OSE} of the Arctic observations for medium range forecasts is examined by composite maps of OI_{OSE} during Days 0.25–3 and Days 4–7 (medium ranges) for the 4 Arctic OSEs (Figs. 12a,b). During the short range, beneficial Arctic OI_{OSE} originating from the initial observation points amplifies within the Arctic regions (Fig. 12a). In the medium range, areas of beneficial OI_{OSE} are found at the east coast of North America and over the northeastern Pacific in the midlatitudes (Fig. 12a). The former area is possibly due to dynamical propagation of the initial Arctic

OI_{OSE} . The dynamical propagation is partly illustrated by vertically averaged flux of OI_{OSE} for the Arctic OSEs as composite of $\mathbf{v} \Delta E_{exp}^2(t)$ where \mathbf{v} is wind vectors of the CTL. We can find that the flux is from the eastern Hemisphere of the Arctic Circle toward the eastern coastal region of North America during short- to medium ranges (Figs. 12a,b). The flux pattern supports the existence of the dynamical propagation toward the midlatitudes. It should be noted the flux just visualizes one aspect of the propagation, i.e., propagation in the Lagrangian way.

To further examine the dynamical propagation, we plot the time evolution of the $\Delta E_{exp}^2(t)$ box-budgets over the Arctic and over the midlatitude north American domains for each OSE (Fig. 13). We find amplifications of the initial beneficial OI_{OSE} for the Pol, Pol2, and Pol4 experiments in the Arctic domain during Days 2–4. After the amplifications, beneficial OI_{OSE} for the same experiments appear in the midlatitude (North American) domain during short and early medium ranges (Days 1–4) and during the late-medium range (Days 6–7). On the other hand, for the Pol3 experiment in which initial OI_{OSE}

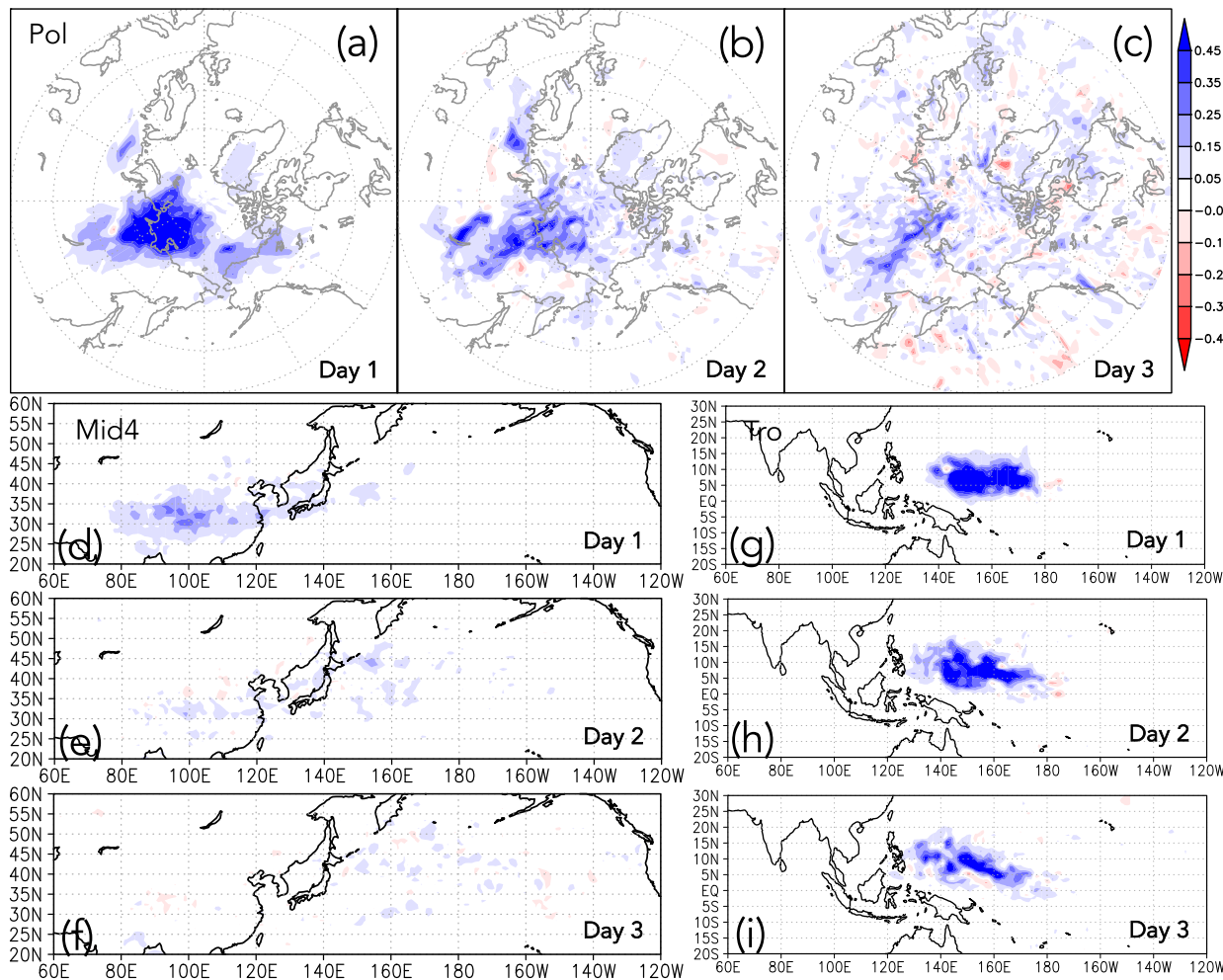


FIG. 10. As in Fig. 9, but for $OI_{EFSO} \Delta \epsilon_{exp}^2(t)$ ($J \text{ kg}^{-1}$).

and OI_{EFSO} are smallest (most non-beneficial) among the Arctic OSEs, the amplification in the Arctic domain is much weaker and no beneficial OI_{OSE} appear in the midlatitude domain. These results also support the existence of the dynamical propagation of the Arctic OI_{OSE} in the medium range, and show that the Arctic observations with more beneficial initial OI_{OSE} can have more beneficial OI_{OSE} regions within the Arctic Circle and in middle North America in the medium range. Since the initial Arctic OI_{OSE} can be estimated by OI_{EFSO} , EFSO for the Arctic observations are useful even for the medium-range forecasts.

Note that there can be two possible major propagation routes for the Arctic OI_{OSE} over North America. One is along the surface. This propagation can be caused by meridional direct circulations in the extratropics; this is suggested by the pattern of $\mathbf{v} \Delta E_{exp}^2(t)$ being similar to the North American stream of cold air mass flux (Iwasaki et al. 2014, their Fig. 5). This flux is calculated based mass-weighted isentropic means (MIM, Iwasaki 1989; Iwasaki and Mochizuki 2012), and has been shown to describe the Lagrangian mean meridional circulation and Northern Hemisphere cold air outbreaks (Kanno

et al. 2015). The other major route is along the upper troposphere. This upper-level propagation can be via both phase and/or group velocity of Rossby waves (Takaya and Nakamura 2001) and Lagrangian potential-vorticity advection (Yamazaki and Itoh 2013). Such propagation can be enhanced along climatologically strong potential-vorticity gradient zones (i.e., waveguides) in the upper troposphere. Although the Rossby-wave propagation cannot be expressed by the $\mathbf{v} \Delta E_{exp}^2(t)$ flux, a strong gradient zone exists just over North America starting from east of Alaska (northern North America) to east of middle North America (e.g., Yamazaki et al. 2019, their Fig. 5d). Sato et al. (2020b) reported that importance of the upper-level propagation of Arctic observation impacts. Their relative contributions and quantification of OI_{OSE} propagation should be investigated in future studies.

In addition, the composite map in the medium range for the Arctic OSEs evidently shows different features than those in the midlatitude and tropical OSEs (Figs. 12b–d); areas of beneficial OI_{OSE} are found within the Arctic Circle and at the east coast of middle North America. For the midlatitude and

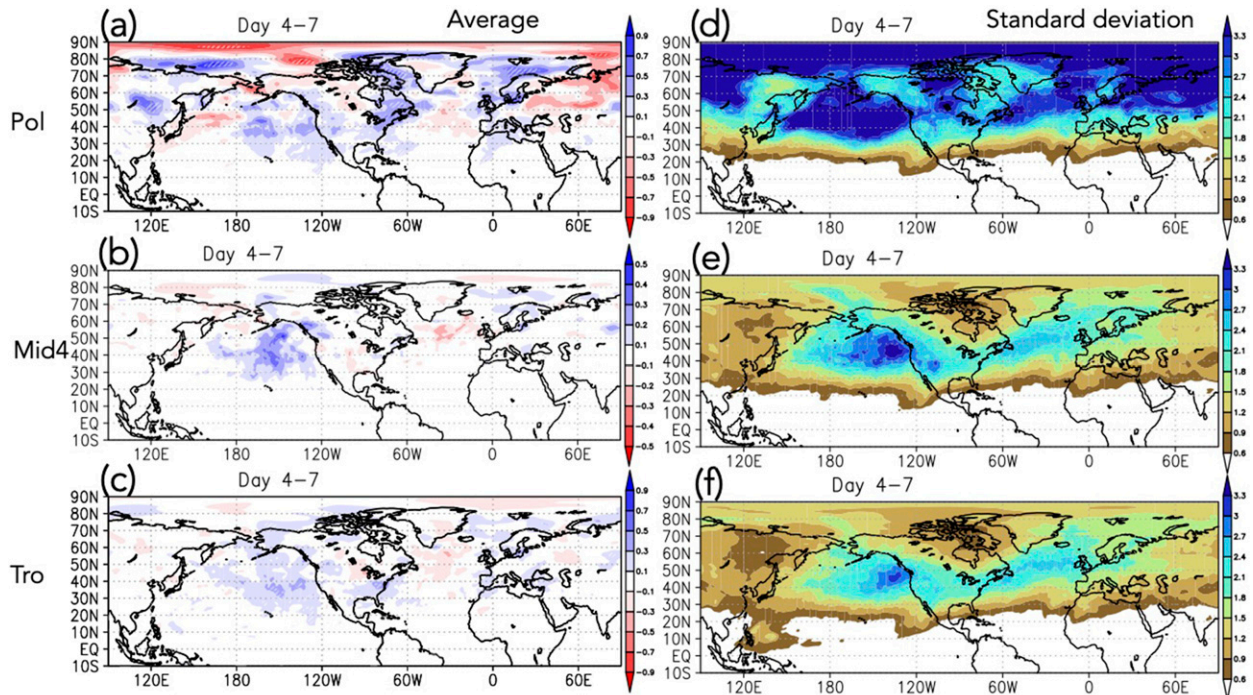


FIG. 11. (a)–(c) As in Fig. 9 but for the averaged OI_{OSE} during days 4–7 (medium ranges) for (a) $\Delta E_{Pol}^2(t)$, (b) $\Delta E_{Mid4}^2(t)$, and (c) $\Delta E_{Tro}^2(t)$. The hatching indicates statistical confidence exceeding 90%. (d)–(f) Standard deviations of the averaged $\Delta E_{exp}^2(t)$ ($J\ kg^{-1}$) for the (d) Pol, (e) Mid4, and (f) Tro experiments.

tropical OSEs, an area of the beneficial OI_{OSE} is found over the northeastern Pacific; however, such beneficial area is also found for the Arctic composite map. Therefore, the beneficial OI_{OSE} area over the northeastern Pacific is not related to dynamical propagation.

In summary, the following points are found.

- OI_{OSE} are able to dynamically propagate during short-range forecasts, irrespective of latitude.

- For the medium-range forecasts, the Arctic OI_{OSE} most effectively amplify and dynamically propagate.
- Areas of systematic beneficial OI_{OSE} during medium-range forecasts over the Arctic circle and the east coast of middle North America are associated with Arctic observations.

For the dynamical propagation, the Arctic OI_{OSE} can be mediated by the extratropical direct meridional circulation

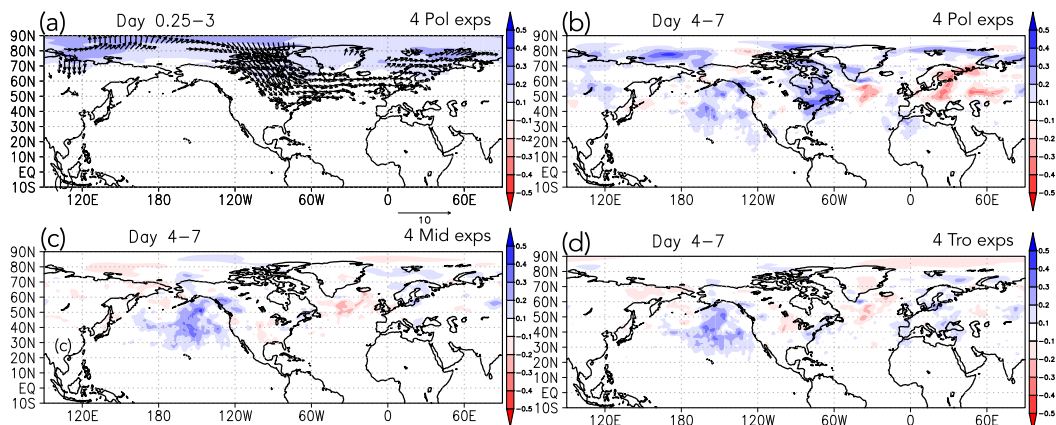


FIG. 12. Composites of the averaged $OI_{OSE} \Delta E_{exp}^2(t)$ ($J\ kg^{-1}$) during (a) days 0.25–3 and (b) days 4–7 (medium ranges) for the four Arctic (Pol, Pol2, Pol3, and Pol4) experiments. The arrows in (a) indicate the flux of the $OI_{OSE} \nabla \Delta E_{exp}^2(t)$ ($J\ kg^{-1}\ m\ s^{-1}$) (see text for more details). (c), (d) As in (b), but the composites for the four midlatitude (Mid, Mid2, Mid3, and Mid4) and the four tropical (Tro, Tro2, Tro3, and Tro4) experiments, respectively.

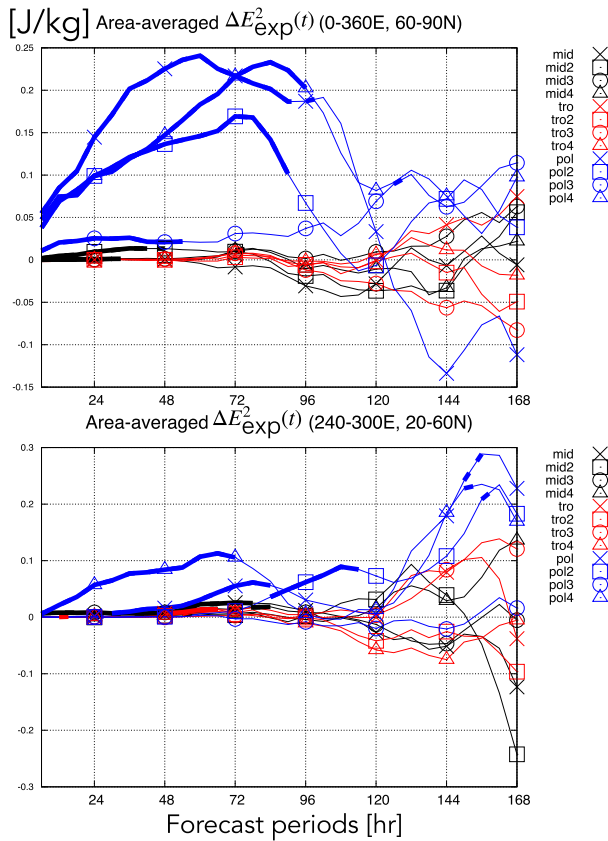


FIG. 13. Time sequences of the area-averaged $OI_{OSE} \Delta E_{exp}^2(t)$ within (top) the Arctic ($0^\circ\text{--}360^\circ\text{E}$, $60^\circ\text{--}90^\circ\text{N}$) and (bottom) the midlatitude North American ($240^\circ\text{--}300^\circ\text{E}$, $20^\circ\text{--}60^\circ\text{N}$) domains. Thick solid and dashed lines indicate statistical confidence exceeding 95% and 90% levels, respectively.

(Iwasaki et al. 2014) and Rossby waves in the upper troposphere: These OI_{OSE} are amplified before reaching the midlatitudes.

c. Discussion: Comparison with repeated OSEs for the Arctic experiments

Finally we discuss how the results above can provide useful information when observations over a limited geographical region are repeatedly collected, which is common in field campaigns. In this case, OI_{OSE} accumulate in the analysis field (e.g., Yamazaki et al. 2015; Sato et al. 2020b). Here we test the Arctic observations because the Arctic OI_{OSE} can most effectively amplify and propagate OI_{OSE} in the short- and medium-range forecasts.

In section 3, the data denial was not repeated for any OSE (non-repeated OSEs hereafter). Here, we conduct two additional data assimilation and forecast experiments for each Arctic OSE, namely the repeated OSE (rep-OSE) and the semi CTL (semi-CTL) forecast experiments. Here, the rep-OSEs are conducted for the Pol, Pol2, Pol3, and Pol4 observations. For example, the rep-Pol analysis is the same analysis of ALERA2 (red arrow in Fig. 4) except the Pol observations for every 0000 UTC (rep-Pol analysis). In the rep-OSE analysis,

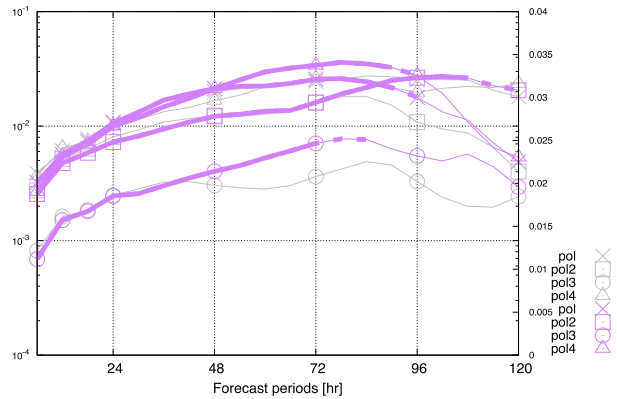


FIG. 14. As in Fig. 8a, but for the repeated (purple lines) and the non-repeated (gray lines) Arctic OSEs. Note that the displayed forecast periods are from 6 h to 5 days.

data denials are repeated during the winter. The semi-CTL analysis is generated from the rep-OSE analysis but with one data-assimilation process for adding the OSE (e.g., Pol) observations every day at 0000 UTC (semi-CTL analysis). This is similar to generating a non-repeated OSE analysis, as described in section 3 (blue circles in Fig. 4). As in the non-repeated OSE, 7-day forecast experiments are conducted initialized with the rep-OSE and the semi-CTL analyses at every 0000 UTC during winter (91 times for each forecast experiment). The $OI_{rep-OSE} [\Delta \overline{E_{rep-exp}^2}(t) \text{ or } \Delta E_{rep-exp}^2(t)]$ is calculated as the forecast difference between semi-CTL $\mathbf{x}_{semi-CTL}^f(t)$ and rep-OSE $\mathbf{x}_{rep-OSE}^f(t)$ using Eqs. (5) and (3), where $\mathbf{x}_{semi-CTL}^f(t)$ and $\mathbf{x}_{rep-OSE}^f(t)$ correspond to $\mathbf{x}_{CTL}^f(t)$ and $\mathbf{x}_{OSE}^f(t)$ in the (non-repeated) OSE experiment, respectively. By comparing $OI_{rep-OSE}$ with OI_{OSE} , we can assess whether the results obtained by a non-repeated OSE allows estimating the impact obtained by a repeated OSE.

Time sequences of $\Delta \overline{E_{rep-exp}^2}(t)$ and $\Delta E_{exp}^2(t)$ are plotted in Fig. 14. During the short-range forecast (6–36 h), $\Delta \overline{E_{rep-exp}^2}(t)$ and $\Delta E_{exp}^2(t)$ are similar, though $\Delta \overline{E_{rep-exp}^2}(t=6)$ are slightly smaller than $\Delta E_{exp}^2(t=6)$. In particular, this similarity remains true up to 72 h (early medium range) for the rep-Pol and rep-Pol2 experiments. The relative differences (rankings) of 6-h (initial) $OI_{rep-OSE}$ almost retains unchanged up to Day 2. In particular, the difference between $\Delta \overline{E_{rep-exp}^2}(t)$ and the other $\Delta \overline{E_{rep-exp}^2}(t)$ is kept until Day 5. These are similar with the non-repeated Arctic OSEs, suggesting that EFSO for the (non-repeated) Arctic OSEs can also be useful to estimate the Arctic $OI_{rep-OSE}$ in short-range forecasts.

Amplification and dynamical propagation of $\Delta E_{rep-exp}^2(t)$ including the medium-range period are evaluated by examining the composite maps averaged over Days 0.25–3 and Days 4–7 (Fig. 15). The maps are compared with those of the Arctic $\Delta E_{exp}^2(t)$ maps (Figs. 12a,b). The $OI_{rep-OSE}$ map during the short range shows very similar patterns with the OI_{OSE} map (Fig. 12a). Furthermore, the $OI_{rep-OSE}$ distribution in the medium range shows the similar beneficial areas in middle North America and within the Arctic Circle to those in the Arctic OI_{OSE} map (Fig. 12b). Therefore, the same mechanism (amplification and

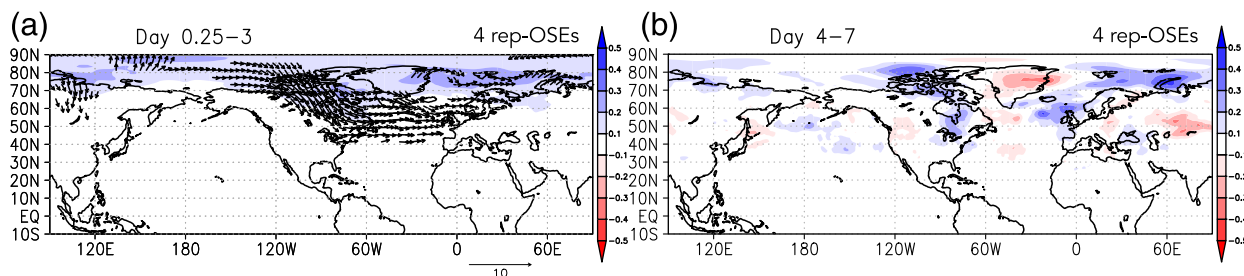


FIG. 15. As in Figs. 12a and 12b, but for the repeated Arctic OSEs.

dynamical propagation) in the non-repeated Arctic OSEs can be adopted to the repeated Arctic OSEs.

Interestingly, the beneficial regions of $OI_{rep-OSE}$ and OI_{OSE} are consistent with Jung et al. (2014), in which the influence of Arctic atmospheric reproducibility (observation impact) improved the medium-range forecast in the midlatitudes, especially in North America (their Fig. 2).

Therefore, non-repeated OSEs and their OI_{EFSO} can provide useful information on the outcome of repeated OSEs, such as obtained during long-term observational campaigns. It would be interesting topic for future studies to compare repeated and non-repeated OSEs in other latitudinal bands.

5. Conclusions

We have successfully implemented the EFSO technique in the AFES-LETKF data assimilation system (ALEDAS). Based on this system, we have investigated whether the 6-h EFSO diagnosis can approximate the results of OSEs.

We conducted 12 OSEs in each of which a subset of radiosondes launched at three neighboring sites was excluded from the data assimilation. To obtain the observation impacts (OI_{OSE}), we compared these experiments with the control experiment, in which all radiosondes were included. The 12 observation sites were selected from the Northern Hemisphere (4 in the Arctic, 4 in the midlatitudes, and 4 in the tropics). Through non-repeated data-denial experiments for the winter (December–February) of 2015/16, we have examined to what extent the 6-h OI_{OSE} obtained by the OSEs are estimated by the EFSO technique. Our results suggest that the winter-averaged EFSO technique can accurately estimate 6-h OI_{OSE} in all three latitude bands (Arctic, midlatitudes, tropics).

We have also tested whether the observation impacts estimated by EFSO (OI_{EFSO}) obtain at lead time 6 h can provide information on OI_{OSE} at short- (1–2 day) and medium-range (3–7 day) forecasts. For short-range forecasts, EFSO well estimated OI_{OSE} at all latitudes. Furthermore, by focusing on spatial distribution of OI_{OSE} , Arctic OI_{OSE} in the short range tended to amplify within the Arctic. During the medium range, these OI_{OSE} dynamically propagated and remained beneficial over several regions: the Arctic Circle and the eastern coastal region of middle North America. Therefore, we conclude that the EFSO technique can be useful to estimate OI_{OSE} in short-range forecasts at all latitudes, and in medium-range forecasts for the Arctic. We have also performed four repeated Arctic OSEs that mimicked Arctic field campaigns covering the

winter period. The results showed consistent evolution and dynamical propagation of Arctic observation impacts obtained from the repeated OSEs that are similar to OI_{OSE} from the non-repeated OSEs. This implies that the results from the non-repeated Arctic OSEs and estimations by EFSO can provide valuable information for repeated Arctic observation campaigns of YOPP.

In other words, our results show that, for medium-range forecasts, the Arctic observations can be the most influential. They can have therefore the highest potential for improving medium-range forecasts in the Northern Hemisphere. Based on the discussion in sections 4b and 4c, we summarize the factors why the Arctic observations can be the most influential.

- 1) The small number of Arctic observations. The Arctic regions are still relatively poorly observed (e.g., Jung et al. 2016, and Fig. 16a). Thus, Arctic observations tend to have a relatively large OI_{EFSO} (Fig. 16c). We note, however, that the tropospheric observation density (observations per km^2), is not very different between the Arctic and tropics (Fig. 16b).
- 2) Due to the existence of the extratropical direct meridional circulation toward the midlatitudes and due to the ubiquitous Rossby waves in the extratropical upper troposphere, the Arctic OI_{OSE} propagate toward the midlatitudes.
- 3) Choice of error norm (metric) for quantifying OI_{EFSO} and OI_{OSE} . We chose the globally averaged moist total energy, which may emphasize errors on midlatitude storm-track regions (Figs. 11d–f). This choice is motivated by our interest in the midlatitude storm tracks, which are one of the most important elements of the general circulation.

In this paper, AFES, a typical atmospheric general circulation model with moderate horizontal and vertical resolution and a hydrostatic dynamical core, is used. The model is sufficient for our purposes, since we have used AFES and ALEDAS to conduct weather predictability studies for synoptic–large-scale atmospheric circulations (Yamazaki et al. 2015; Inoue et al. 2015; Sato et al. 2017; Kawai et al. 2017; Sato et al. 2018a,b, 2020a,b). In addition, high-resolution and convection-permitting forecast models can better represent the dynamical propagation, compared with trivial numerical errors; this is because the high-resolution models are more realistic. In short, while the former has a realistic process, the latter is due to unrealistic numerical noises. Convection-permitting models can reproduce more realistic tropical OI_{OSE} and dynamical propagation; these may be underestimated in this study. Ensemble forecasting with more members can also reduce the

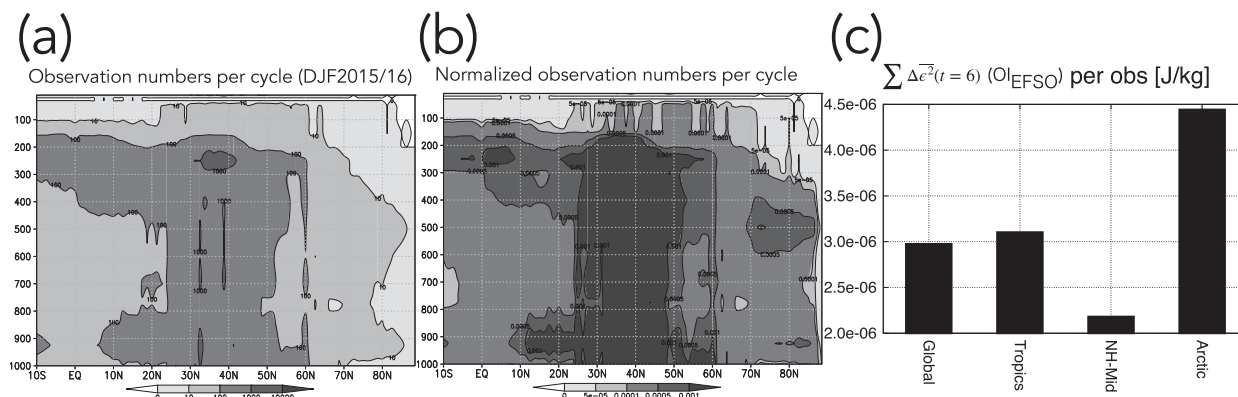


FIG. 16. Latitude–height cross section of (a) observation numbers per cycle and (b) its density distribution used in ALERA2 in free atmosphere (above 1000 hPa) during winter. In the density distribution in (b), the numbers normalized by areas (weighted by $\cos^{-1}\theta$, where θ is latitude) are displayed. (c) $\sum \Delta \epsilon^2$ and area-separated $\sum \Delta \epsilon^2$ per observation (J kg^{-1}) of the global, the tropical (10°S – 20°N), the Northern Hemisphere midlatitude (20° – 60°N), and the Arctic (60° – 90°N) latitudinal bands.

trivial errors. Note that recent studies using the ECMWF forecast system have highlighted the importance of the Arctic observation impacts on the midlatitude weather systems in medium-range forecasts (Jung et al. 2014; Lawrence et al. 2019; Day et al. 2019). In addition, our results pertain to weekly weather (from 6 h to 7 days) and its impacts on the global domain. The relative importance of observations in the Arctic, midlatitudes, and tropics may vary for longer forecast periods and also vary by region (cf. Zhang et al. 2019).

Acknowledgments. The authors thank the organizer and the participants of the workshop ‘‘Observational Campaigns for Better Weather Forecasts’’ held at ECMWF in June 2019 (Magnusson and Sandu 2019), which inspired and helped us summarize the paper. We are grateful to Dr. Ingo Richter for his thoughtful comments to improve the paper and English language assistance. We also would like to thank three anon-

ymous reviewers, and Drs. Daisuke Hotta and Yoichiro Ota for their helpful comments. The ALERA2 dataset is available from <http://www.jamstec.go.jp/alera/alera2.html>. This work was supported by JSPS KAKENHI (26282111, 15H02129, 17K05663, 18K13617, 18H03745, 18KK0292, and 19H05702), and the Arctic Challenge for Sustainability Research Project (ArCS) by MEXT. Numerical simulations were conducted on the Earth Simulator with the support of JAMSTEC.

APPENDIX A

ALEDAS

The ALEDAS configuration used in the present study is described in Yamazaki et al. (2015): The horizontal resolution is T119, which roughly corresponds to a $1^{\circ} \times 1^{\circ}$ latitudinal and longitudinal horizontal resolution. There are 48 vertical levels,

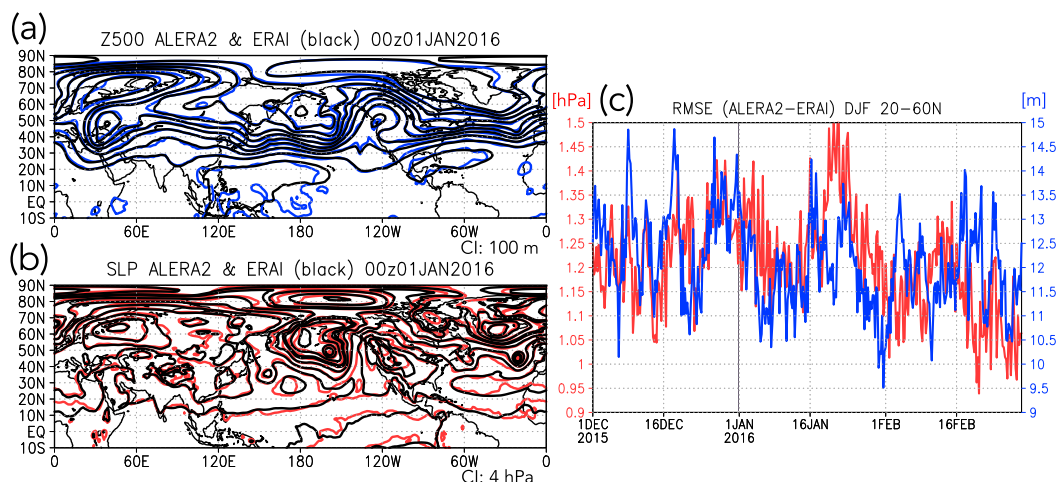


FIG. A1. Snapshots of (a) 500-hPa geopotential height (Z500) and (b) sea level pressure (SLP) fields in ALERA2 (blue or red contours) and ERA-Interim (black contours; Dee et al. 2011) at 0000 UTC 1 Jan 2016. Contour intervals in (a) and (b) are 100 m and 4 hPa, respectively. (c) Root-mean-square differences of Z500 [right axis (m), blue] and SLP [left axis (hPa), red] for the period of December–February in 2015/16. Black vertical line indicates the date shown in (a) and (b).

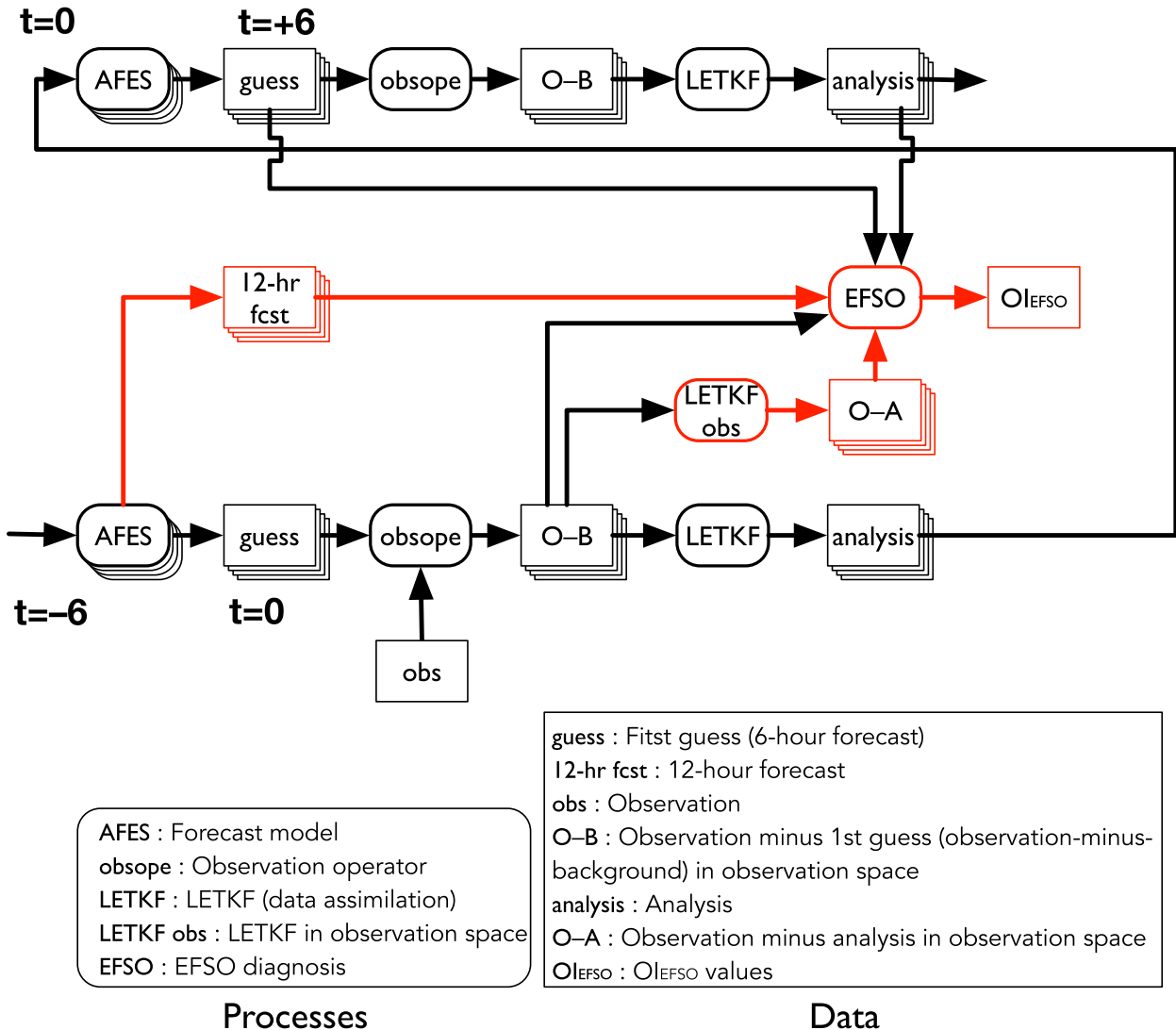


FIG. A2. Flowchart of forecast–analysis cycles in ALEDAS from the analyzed times $t = 0$ and $t = +6$ h. Squared and rounded-corner boxes indicate inputs and outputs (data) and the executed processes, respectively. Details of each process and data are shown in bottom. In this figure, $\mathbf{X}_{t=6|0}^f$ in Eq. (2) is obtained from “guess,” $\mathbf{e}_{t=6|0}$ is from “guess” and “analysis,” $\mathbf{e}_{t=6|-6}$ is from “12-hr fcst” and “analysis,” $\delta\mathbf{y}_0^{\text{ob}}$ and \mathbf{R} are from “O-B,” and \mathbf{Y}_0^a is from “O-A,” respectively. The process “obsope” corresponds to the observation operator H to obtain $\delta\mathbf{y}_0^{\text{ob}}$. Parallel process and ensemble data are shown with additional three boxes. Red indicates newly implemented processes and added outputs for the EFSO diagnosis.

with the top at 3 hPa. The ensemble size is 63. The uniform multiplicative 10% inflation method is used. The horizontal and vertical localization scales of the LETKF are set to 400 km and $0.4\ln p$, respectively (Miyoshi et al. 2007; Enomoto et al. 2013; Yamazaki et al. 2017). Observations include conventional types and satellite winds, which are prepared from the PREPBUFR datasets, compiled by the National Centers for Environmental Prediction (NCEP) and archived at University Corporation for Atmospheric Research (UCAR). ALERA2 can reasonably well reproduce the observed synoptic–large-scale atmospheric circulations (Fig. A1). Further details of ALEDAS and ALERA2 can be found in Miyoshi and Yamane (2007), Enomoto et al. (2013), and Yamazaki et al. (2017).

ALEDAS has been used to evaluate impacts of observations obtained in observational campaigns in various regions for various seasons; the Arctic Ocean (Inoue et al. 2013; Yamazaki et al. 2015; Sato et al. 2017, 2018b, 2020b), midlatitudes (Kawai et al. 2017; Sato et al. 2020b), the Philippine Sea (Hattori et al. 2017), the Southern Ocean (Sato et al. 2018a), and the Antarctic (Sato et al. 2020a) during summer (Yamazaki et al. 2015; Kawai et al. 2017; Sato et al. 2018a,b, 2020a), fall (Inoue et al. 2013; Hattori et al. 2017; Sato et al. 2020b), and winter (Sato et al. 2017).

Flowchart of forecast–analysis cycles in ALEDAS are shown in Fig. A2. In terms of code modifications to calculate the 6-h EFSO diagnosis, we must additionally calculate \mathbf{Y}_0^a and

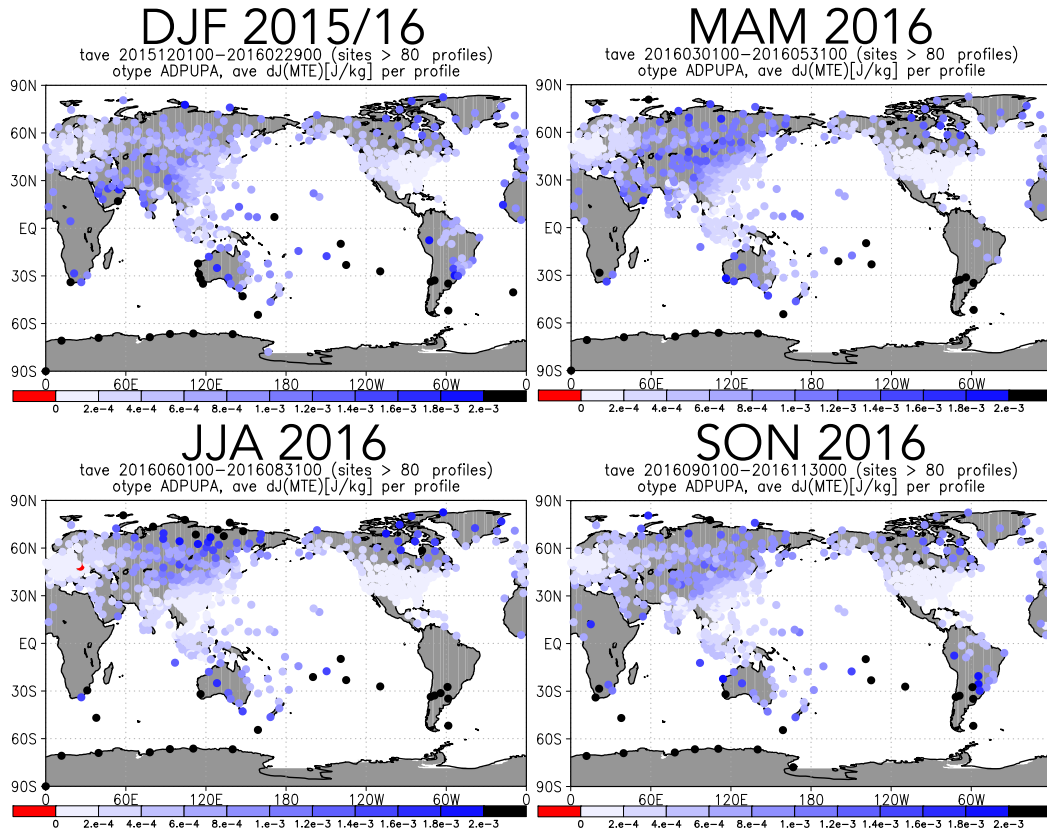


FIG. B1. As in Fig. 3 but for all the seasons during (top left) winter 2015/16, (top right) spring 2016, (bottom left) summer 2016, and (bottom right) fall 2016. Seasonal averages of $\Delta\epsilon^2(t=6)$ (J kg^{-1}) are displayed. Only radiosonde observations for locations that reported more than 80 times at 0000 UTC during each season are shown. The wind fields are not displayed here.

e_{t-6} in the ALEDAS flowchart, to output OI_{EFSO} . Additional processes that one uses to calculate the OI_{EFSO} values are (i) extended forecasts for 3 h in addition to the 9-h forecast of the 4-D LETKF process (i.e., the “12-hour forecast” process in Fig. A2), (ii) calculation of \mathbf{Y}^a , and (iii) calculation of OI_{EFSO} . We consider that these additional processes are minimal and

optimal for our system because the computational cost of 9-h ensemble forecasting (forecast) is more than twice that for the LETKF (analysis) in the original ALEDAS cycle (denoted by black in Fig. A2) and the EFSO calculation requires as much time as the LETKF. Those choices make the technique more suitable for the use in observational campaigns with limited resources.

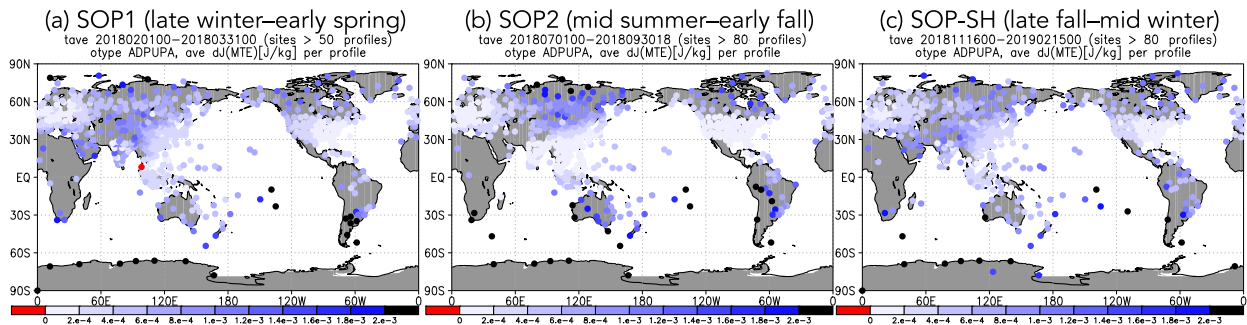


FIG. B2. As in Fig. B1, but for special observing periods (SOPs) of YOPP when frequencies of radiosonde observations in (a), (b) the Arctic and (c) the Antarctic regions were increased at many routine stations. The SOPs are from 1 Feb 2018 to 31 Mar 2018 in (a), from 1 Jul 2018 to 30 Sep 2018 in (b), and from 16 Nov 2018 to 15 Feb 2019 in (c). Averaged values of $\Delta\epsilon^2(t=6)$ during the SOPs (J kg^{-1}) are displayed. Note that only radiosonde observations for locations that reported more than 50 [in (a)] and 80 times [in (b) and (c)] at 0000 UTC during each SOP are shown.

APPENDIX B

Seasonal OI_{EFSO} Values and the Values during the Special Observing Periods

ALEDAS and the EFSO diagnosis continued until winter 2019. We show the seasonality of OI_{EFSO} for the whole globe. Figure B1 shows the seasonal averages of the OI_{EFSO} values of the radiosondes. We can find two features common to all seasons: (i) the OI_{EFSO} values are smoothly distributed, and (ii) the OI_{EFSO} values are larger in the higher latitudes.

The same features are found in the maps during special observing periods (SOPs) of the Year of Polar Prediction (YOPP, Jung et al. 2016; Bromwich et al. 2020) when the extra radiosonde observations were performed (i.e., the polar observations were extremely increased) at many routine stations and mobile stations by field campaigns in the Arctic or Antarctic regions (Fig. B2).

REFERENCES

Ancell, B. C., A. Bogusz, M. J. Lauridsen, and C. J. Nauert, 2018: Seeding chaos: The dire consequences of numerical noise in NWP perturbation experiments. *Bull. Amer. Meteor. Soc.*, **99**, 615–628, <https://doi.org/10.1175/BAMS-D-17-0129.1>.

Bormann, N., H. Lawrence, and J. Farnan, 2019: Global observing system experiments in the ECMWF assimilation system. Tech. Rep. 839, ECMWF, European Centre for Medium-Range Weather Forecasts Shinfield Park, Reading, United Kingdom, 24 pp, <https://doi.org/10.21957/sr184iyz>.

Bromwich, D. H., and Coauthors, 2020: The Year of Polar Prediction in the Southern Hemisphere (YOPP-SH). *Bull. Amer. Meteor. Soc.*, **101**, 1653–1676, <https://doi.org/10.1175/BAMS-D-19-0255.1>.

Cardinali, C., 2018: Forecast sensitivity observation impact with an observation-only based objective function. *Quart. J. Roy. Meteor. Soc.*, **144**, 2089–2098, <https://doi.org/10.1002/qj.3305>.

Day, J., I. Sandu, L. Magnusson, M. Rodwell, H. Lawrence, N. Bormann, and T. Jung, 2019: Increased arctic influence on the mid-latitude flow during Scandinavian blocking episodes. *Quart. J. Roy. Meteor. Soc.*, **145**, 3846–3862, <https://doi.org/10.1002/qj.3673>.

Dee, D. P., and Coauthors, 2011: The ERA-Interim reanalysis: Configuration and performance of the data assimilation system. *Quart. J. Roy. Meteor. Soc.*, **137**, 553–597, <https://doi.org/10.1002/qj.828>.

Enomoto, T., T. Miyoshi, Q. Moteki, J. Inoue, M. Hattori, A. Kuwano-Yoshida, N. Komori, and S. Yamane, 2013: Observing-system research and ensemble data assimilation at JAMSTEC. *Data Assimilation for Atmospheric, Oceanic and Hydrologic Applications (Vol. II)*, S. Park and L. Xu, Eds., Springer, 509–526, https://doi.org/10.1007/978-3-642-35088-7_21.

Gelaro, R., and Y. Zhu, 2009: Examination of observation impacts derived from observing system experiments (OSEs) and adjacent models. *Tellus*, **61A**, 179–193, <https://doi.org/10.1111/j.1600-0870.2008.00388.x>.

Hattori, M., A. Yamazaki, S.-Y. Ogino, P. Wu, and J. Matsumoto, 2017: Impact of the radiosonde observations of cold surge over the Philippine Sea on the tropical region and the Southern Hemisphere in December 2012. *SOLA*, **13**, 19–24, <https://doi.org/10.2151/sola.2017-004>.

Hodys, D., and S. J. Majumdar, 2007: The contamination of ‘data impact’ in global models by rapidly growing mesoscale

instabilities. *Quart. J. Roy. Meteor. Soc.*, **133**, 1865–1875, <https://doi.org/10.1002/qj.157>.

Hoskins, B. J., and K. I. Hodges, 2002: New perspectives on the Northern Hemisphere winter storm tracks. *J. Atmos. Sci.*, **59**, 1041–1061, [https://doi.org/10.1175/1520-0469\(2002\)059<1041:NPTNH>2.0.CO;2](https://doi.org/10.1175/1520-0469(2002)059<1041:NPTNH>2.0.CO;2).

Hotta, D., 2014: Proactive quality control based on ensemble forecast sensitivity to observations. Ph.D. thesis, University of Maryland, 248 pp.

—, T.-C. Chen, E. Kalnay, Y. Ota, and T. Miyoshi, 2017: Proactive QC: A fully flow-dependent quality control scheme based on EFSO. *Mon. Wea. Rev.*, **145**, 3331–3354, <https://doi.org/10.1175/MWR-D-16-0290.1>.

Inoue, J., T. Enomoto, and M. E. Hori, 2013: The impact of radiosonde data over the ice-free Arctic Ocean on the atmospheric circulation in the Northern Hemisphere. *Geophys. Res. Lett.*, **40**, 864–869, <https://doi.org/10.1002/grl.50207>.

—, A. Yamazaki, J. Ono, K. Dethloff, M. Maturilli, R. Neuber, P. Edwards, and H. Yamaguchi, 2015: Additional Arctic observations improve weather and sea-ice forecasts for the Northern Sea Route. *Sci. Rep.*, **5**, 16868, <https://doi.org/10.1038/srep16868>.

Ito, K., and Coauthors, 2018: Analysis and forecast using dropsonde data from the inner-core region of tropical cyclone Lan (2017) obtained during the first aircraft missions of T-PARCII. *SOLA*, **14**, 105–110, <https://doi.org/10.2151/sola.2018-018>.

Iwasaki, T., 1989: A diagnostic formulation for wave–mean flow interactions and Lagrangian-mean circulation with a hybrid vertical coordinate of pressure and isentropes. *J. Meteor. Soc. Japan*, **67**, 293–312, https://doi.org/10.2151/jmsj1965.67.2_293.

—, and Y. Mochizuki, 2012: Mass-weighted isentropic zonal mean equatorward flow in the Northern Hemispheric winter. *SOLA*, **8**, 115–118, <https://doi.org/10.2151/sola.2012-029>.

—, T. Shoji, Y. Kanno, M. Sawada, M. Ujiie, and K. Takaya, 2014: Isentropic analysis of polar cold air mass streams in the Northern Hemispheric winter. *J. Atmos. Sci.*, **71**, 2230–2243, <https://doi.org/10.1175/JAS-D-13-058.1>.

Jung, T., M. A. Kasper, T. Semmler, and S. Serrar, 2014: Arctic influence on subseasonal midlatitude prediction. *Geophys. Res. Lett.*, **41**, 3676–3680, <https://doi.org/10.1002/2014GL059961>.

—, and Coauthors, 2016: Advancing polar prediction capabilities on daily to seasonal time scales. *Bull. Amer. Meteor. Soc.*, **97**, 1631–1647, <https://doi.org/10.1175/BAMS-D-14-00246.1>.

Kalnay, E., Y. Ota, T. Miyoshi, and J. Liu, 2012: A simpler formulation of forecast sensitivity to observations: Application to ensemble Kalman filters. *Tellus*, **64A**, 18462, <https://doi.org/10.3402/tellusa.v64i0.18462>.

Kanno, Y., M. R. Abdillahi, and T. Iwasaki, 2015: Charge and discharge of polar cold air mass in Northern Hemispheric winter. *Geophys. Res. Lett.*, **42**, 7187–7193, <https://doi.org/10.1002/2015GL065626>.

Kawai, Y., Q. Moteki, A. Yoshida-Kuwano, T. Enomoto, A. Manda, and H. Nakamura, 2017: Impact propagation of radiosonde data assimilation over the Kuroshio and Kuroshio Extension: Case study on the early summer (Baiu) in 2012. *J. Meteor. Soc. Japan*, **95**, 71–90, <https://doi.org/10.2151/jmsj.2017-004>.

Kotsuki, S., K. Kurosawa, and T. Miyoshi, 2019: On the properties of ensemble forecast sensitivity to observations. *Quart. J. Roy. Meteor. Soc.*, **145**, 1897–1914, <https://doi.org/10.1002/qj.3534>.

Langland, R. H., and N. L. Baker, 2004: Estimation of observation impact using the NRL atmospheric variational data assimila-

- tion adjoint system. *Tellus*, **56A**, 189–201, <https://doi.org/10.3402/tellusa.v56i3.14413>.
- Lawrence, H., N. Bormann, I. Sandu, J. Day, J. Farnan, and P. Bauer, 2019: Use and impact of Arctic observations in the ECMWF numerical weather prediction system. *Quart. J. Roy. Meteor. Soc.*, **145**, 3432–3454, <https://doi.org/10.1002/qj.3628>.
- Lien, G., D. Hotta, E. Kalnay, T. Miyoshi, and T.-C. Chen, 2018: Accelerating assimilation development for new observing systems using EFSO. *Nonlinear Processes Geophys.*, **25**, 129–143, <https://doi.org/10.5194/npg-25-129-2018>.
- Liu, J., and E. Kalnay, 2008: Estimating observation impact without adjoint model in an ensemble Kalman filter. *Quart. J. Roy. Meteor. Soc.*, **134**, 1327–1335, <https://doi.org/10.1002/qj.280>.
- Magnusson, L., and I. Sandu, 2019: Experts review synergies between observational campaigns and weather forecasting. *ECMWF Newsletter*, No. 161, ECMWF, Reading, United Kingdom, 6–7, <https://www.ecmwf.int/en/newsletter/161/news/experts-review-synergies-between-observational-campaigns-and-weather>.
- Majumdar, S. J., 2016: A review of targeted observations. *Bull. Amer. Meteor. Soc.*, **97**, 2287–2303, <https://doi.org/10.1175/BAMS-D-14-00259.1>.
- Miyoshi, T., and S. Yamane, 2007: Local ensemble transform Kalman filtering with an AGCM at a T159/l48 resolution. *Mon. Wea. Rev.*, **135**, 3841–3861, <https://doi.org/10.1175/2007MWR1873.1>.
- , —, and T. Enomoto, 2007: Localizing the error covariance by physical distances within a Local Ensemble Transform Kalman Filter (LETKF). *SOLA*, **3**, 89–92, <https://doi.org/10.2151/sola.2007-023>.
- Moteki, Q., and Coauthors, 2011: The influence of observations propagated by convectively coupled equatorial waves. *Quart. J. Roy. Meteor. Soc.*, **137**, 641–655, <https://doi.org/10.1002/qj.779>.
- Necker, T., M. Weissmann, and M. Sommer, 2018: The importance of appropriate verification metrics for the assessment of observation impact in a convection-permitting modelling system. *Quart. J. Roy. Meteor. Soc.*, **144**, 1667–1680, <https://doi.org/10.1002/qj.3390>.
- Ota, Y., J. C. Derber, T. Miyoshi, and E. Kalnay, 2013: Ensemble-based observation impact estimates using the NCEP GFS. *Tellus*, **65A**, 20038, <https://doi.org/10.3402/tellusa.v65i0.20038>.
- Privé, N., R. M. Errico, R. Todling, and A. E. Akkroui, 2021: Evaluation of adjoint-based observation impacts as a function of forecast length using an Observing System Simulation Experiment. *Quart. J. Roy. Meteor. Soc.*, **147**, 121–138, <https://doi.org/10.1002/qj.3909>.
- Sato, K., J. Inoue, A. Yamazaki, J. Kim, M. Maturilli, K. Dethloff, S. R. Hudson, and M. A. Granskog, 2017: Improved forecasts of winter weather extremes over midlatitudes with extra Arctic observations. *J. Geophys. Res. Oceans*, **122**, 775–787, <https://doi.org/10.1002/2016JC012197>.
- , —, S. P. Alexander, G. McFarquhar, and A. Yamazaki, 2018a: Improved reanalysis and prediction of atmospheric fields over the Southern Ocean using campaign-based radiosonde observations. *Geophys. Res. Lett.*, **45**, 11 406–11 413, <https://doi.org/10.1029/2018GL079037>.
- , —, A. Yamazaki, J.-H. Kim, A. Makshtas, V. Kustov, M. Maturilli, and K. Dethloff, 2018b: Impact on predictability of tropical and mid-latitude cyclones by extra Arctic observations. *Sci. Rep.*, **8**, 12104, <https://doi.org/10.1038/s41598-018-30594-4>.
- , —, —, N. Hirasawa, K. Sugiura, and K. Yamada, 2020a: Antarctic radiosonde observations reduce uncertainties and errors in reanalyses and forecasts over the Southern Ocean: An extreme cyclone case. *Adv. Atmos. Sci.*, **37**, 431–440, <https://doi.org/10.1007/s00376-019-8231-x>.
- , —, and —, 2020b: Performance of forecasts of hurricanes with and without upper-level troughs over the mid-latitudes. *Atmosphere*, **11**, 702, <https://doi.org/10.3390/atmos11070702>.
- Schäfer, A., and Coauthors, 2018: The North Atlantic waveguide and downstream impact experiment. *Bull. Amer. Meteor. Soc.*, **99**, 1607–1637, <https://doi.org/10.1175/BAMS-D-17-0003.1>.
- Sellwood, K. J., S. J. Majumdar, B. E. Mapes, and I. Szunyogh, 2008: Predicting the influence of observations on medium-range forecasts of atmospheric flow. *Quart. J. Roy. Meteor. Soc.*, **134**, 2011–2027, <https://doi.org/10.1002/qj.341>.
- Sommer, M., and M. Weissmann, 2016: Ensemble-based approximation of observation impact using an observation-based verification metric. *Tellus*, **68A**, 27885, <https://doi.org/10.3402/tellusa.v68.27885>.
- Takaya, K., and H. Nakamura, 2001: A formulation of a phase-independent wave-activity flux for stationary and migratory quasigeostrophic eddies on a zonally varying basic flow. *J. Atmos. Sci.*, **58**, 608–627, [https://doi.org/10.1175/1520-0469\(2001\)058<0608:AFOAPI>2.0.CO;2](https://doi.org/10.1175/1520-0469(2001)058<0608:AFOAPI>2.0.CO;2).
- Weissmann, M., and Coauthors, 2011: The influence of assimilating dropsonde data on typhoon track and midlatitude forecasts. *Mon. Wea. Rev.*, **139**, 908–920, <https://doi.org/10.1175/2010MWR3377.1>.
- Yamazaki, A., and H. Itoh, 2013: Vortex–vortex interactions for the maintenance of blocking. Part I: The selective absorption mechanism and a case study. *J. Atmos. Sci.*, **70**, 725–742, <https://doi.org/10.1175/JAS-D-11-0295.1>.
- , J. Inoue, K. Dethloff, M. Maturilli, and G. König-Langlo, 2015: Impact of radiosonde observations on forecasting summertime Arctic cyclone formation. *J. Geophys. Res. Atmos.*, **120**, 3249–3273, <https://doi.org/10.1002/2014JD022925>.
- , T. Enomoto, T. Miyoshi, A. Kuwano-Yoshida, and N. Komori, 2017: Using observations near the poles in the AFES-LETKF data assimilation system. *SOLA*, **13**, 41–46, <https://doi.org/10.2151/sola.2017-008>.
- , M. Honda, and H. Kawase, 2019: Regional snowfall distributions in a Japan-Sea side area of Japan associated with jet variability and blocking. *J. Meteor. Soc. Japan*, **97**, 205–226, <https://doi.org/10.2151/jmsj.2019-012>.
- Zhang, F., Y. Q. Sun, L. Magnusson, R. Buizza, S.-J. Lin, J.-H. Chen, and K. Emanuel, 2019: What is the predictability limit of midlatitude weather? *J. Atmos. Sci.*, **76**, 1077–1091, <https://doi.org/10.1175/JAS-D-18-0269.1>.